Spatial distribution analysis and three-dimensional seismic slope stability assessment of coseismic landslides

--an application to the 2018 Eastern Iburi Earthquake, Hokkaido, Japan—

Shuai ZHANG

2019

博士論文

Spatial distribution analysis and three-dimensional seismic slope stability assessment of coseismic landslides

--an application to the 2018 Eastern Iburi Earthquake, Hokkaido, Japan--

SHUAI ZHANG

平成28年度入学

島根大学大学院総合理工学研究科博士後期課程

総合理工学専攻 地球科学・地球環境　コース

主指導教員：汪 発武

令和元年 7 月 30 日

ABSTRACT

Generally, catastrophic earthquakes are accompanied or followed by large numbers of concurrent landslides, and inflict a high number of casualties and extensive damage of houses and infrastructures. In the last three decades, several strong earthquakes occurred in Japan and numerous secondary geohazards were triggered during the mainshock and aftershocks. Japan is located in one of the most tectonically active regions in the world due to the subductions of Philippine Sea Plate and Pacific Plate to the Eurasian plates and the convergence between the North American and Eurasian Plates. Numerous earthquakes occurred in history and triggered substantial slope failures. The 1995 great Hyogoken-Nambu earthquake (Mw 6.9) induced 674 landslides within an area of about 700 km^2 and was responsible for 6,289 fatalities. 3,467 coseismic landslides were resulted and 50 people were killed in the 2016 Kumamoto earthquake sequence.

The 2018 Hokkaido Eastern Iburi earthquake (Mj 6.7, Mw 6.6), occurred on the 6th of September 2018 in eastern Iburi regions of Hokkaido, Northern Japan one day after the Typhoon Jebi passed through the region. Thousands of landslides were triggered and significant losses resulted from the earthquake sequence and thirty-six people were killed by the landslides despite the afflicted area being sparsely populated. In addition, a sequence of persistent aftershocks occurred, even though the regional seismicity attenuated thereafter. The Iburi region is prone to major earthquake in the future. Thus, studies on spatial distribution analysis of coseimic landslides and seismic slope stability assessment of pyroclastic fall deposits are of great importance for understanding the characteristics of the Iburi landslides. Moreover, these studies can provide a macroscopic perspective for further research and hazards mitigation during a similar scenario in future.

Based on the on-site field reconnaissance in September 2018, it was confirmed that most of the coseismic landslides are translational landslides of small to medium scale with high mobility and long run-out distance. Coherent shallow debris slide and disrupted mobilization of valley fill are two main types of slope failures. Slope failures were triggered in stratified pyroclastic fall deposits, in the combination of strong seismic ground motion and intense antecedent precipitation. In addition, sliding zone liquefaction phenomena were observed during the field investigation.

In this work, a complete coseismic landslide inventory covering almost all the Iburi landslides was delineated. On the basis of coseismic landslide inventory, the spatial distribution of the Iburi landslides and factors controlling the occurrence of the slope failures were analyzed. It is found that all the 5,625 landslides spread in an elliptic area extending NNW/SSE, running approximately parallel to the strike of (active) faults in this region. The preferred aspect of the landslide-affected area is southerly, running nearly perpendicular to the NNW/SSE striking (active) faults. Most coseismic landslides are distributed in regions with seismic intensity of 7.0 to 8.0 (MMI Scale), with peak ground acceleration (PGA) of 0.4 g to 0.7 g. Most of the coseismic landslides occurred at elevations between 100 m and 250 m, and slope angles between 15° and 35°. Miocene sedimentary rock is the predominant bedrock type identified in the landslide area. The relationship between the old landslides (slope failures occurred prior to the Iburi earthquake) and the coseismic landslides is also discussed in this work.

In order to evaluate the seismic stability of slopes in pyroclastic fall deposits, four towns in western Atsuma (Tomisato, Yoshinoya, Sakuraoka and Horosato) where catastrophic landslides occurred, were selected as target area. The source areas and deposition areas of the 345 coseismic landslides in the target area were classified. Based on the isopachs of different pyroclastic fall deposits mantled in the study area, GIS was employed to process the input soil layers and construct the 3D soil structure. By applying different horizontal pseudo-acceleration coefficients in the Scoops3D program, the factor-of-safety maps of eight cases were obtained. After validating with the coseismic landslide inventory, the performance of the computed results was evaluated. A horizontal pseudo-acceleration coefficient between 1/2 and 2/3 of PHGA is suitable for seismic slope stability assessment in pyroclastic fall deposits. The catastrophic Tomisato landslide and Yoshinoya landslide were correctly predicted. Scoops3D proves to be an effective and efficient method for guiding disaster mitigation and management.

ACKNOWLEDGEMENT

The thesis entitled "*Spatial distribution analysis and three-dimensional seismic slope stability assessment of coseismic landslides--an application to the 2018 Eastern Iburi Earthquake, Hokkaido, Japan*--" is written in order to fulfill the partial requirement for the degree of doctor in Department of Earth Science, Interdisciplinary Faculty of Science and Engineering, Shimane University, Japan.

First and foremost, I would like to express my deepest appreciation to my enthusiastic supervisor, Professor Fawu Wang, for his continuous guidance, support, and encouragement throughout my Ph.D. study in Shimane University. His immense ideas, suggestions, and patience give me endless power to overcome difficulties confronted during the research. His tremendous knowledge and positive attitude towards life and research will be lifelong benefits for me.

I wish to express my sincere gratitude to all the professors and staffs in Shimane University, for their academic support and kind help in my Ph.D. study. The "lunch talk" organized by the Department of Earth Science and the field school organized by the International Student Section make my study and life in Japan more colorful and enjoyable.

I am grateful to all members of my dissertation committee for their time on the review and evaluation during the application. The valuable comments and suggests from the dissertation committee are of great help to improve the quality of this thesis.

Many thanks to my Ph.D. fellows, especially all my colleagues in "Swansliders group" from Professor Wang's laboratory in Shimane University for their kind support during this research. I would like to thank professor Zili Dai, Mr. Yoshiharu Yokota, Mr. Akinori Iio, Mr. Prakash Dhungana, Mr. Kounghoon NAM, Ms. Ran Li, and Ms. Rong Zhou. The life, the field works, the seminars and the conferences we shared together will be lifelong reminiscence.

A special acknowledgement goes to the Chinese student community. I was fortune to come across so many Chinese friends in the Chinese student community. Their company and warm help make me accustom to the life in Japan very fast. Thanks for their friendship and kind encouragement.

My deepest gratitude also goes to my parents, my elder sisters and my girlfriend for their moral support. I love them so much, and I would not have made it without their encouragement, help and support. I know I always have my family to count on when times are rough.

I would like to thank the China Scholarship Council (CSC) of the Ministry of Education of the P. R. China for financially supporting my study in Japan. The investigation works in this research were supported by the fund “Initiation and motion mechanisms of long runout landslides due to rainfall and earthquake in the falling pyroclastic deposit slope area” (JSPS-B-19H01980) and the Fundamental Research Grant (2017-2019) of Shimane University on "Development of prediction and mitigation technologies on natural disasters in subduction zone using San-in region as a research field". These financial supports are gratefully acknowledged.

TABLE OF CONTENTS

LIST OF TABLES

LIST OF FIGURES

CHAPTER 1

INTRODUCTION

1.1 Background

Landslides have been recorded for several centuries in Asia and Europe (Schuster 1996) and considered as one of the main natural geohazards causing relevant economic damages and social effects worldwide (Del Soldato et al. 2019). The "cascading down the mountain" inflicted massive casualties and extensive damage on the society. Increased urbanization, heavy precipitation, and strong earthquakes are regarded as the three main triggering factors of landslides. Among these main triggering factors, catastrophic earthquakes are considered to be the most destructive one, as strong earthquakes are generally accompanied or followed by large numbers of concurrent landslides. The casualties and damages resulted from the coseismic landslides are even more severe than those resulted from the earthquakes.

1.1.1 Earthquake-induced landslides in the world

Numerous earthquakes occurred in history and triggered substantial slope failures. In the past decades, several strong earthquakes occurred and numerous secondary geohazards were triggered during the mainshock and aftershocks. The great 1995 Hyogoken-Nambu earthquake (Mw 6.9) induced 674 landslides within an area of about 700 km^2 and was responsible for 6,289 fatalities (Sassa et al. 1996; Fukuoka et al. 1997); the 1999 M_L 7.3 Chi-chi earthquake occurred in the central of Taiwan, resulted in tens of thousands of landslides and accounted for about 2,400 deaths (Wang et al. 2002); More than 15,000 geohazards were generated during the Ms 8.0 Wenchuan earthquake and claimed about 20,000 deaths (Yin et al. 2009); the 2015 Gorkha earthquake sequence occurred in high-elevation and steep-topography areas and induced thousands of landslides, which killed hundreds of people (Collins and Jibson 2015); in the 2016 Kumamoto earthquake sequence 3,467 coseismic landslides were resulted and 50 people were killed (Xu et al. 2018). Understanding spatial distribution characteristics of coseimic landslides occurred in complex seismic, topographic and geological conditions can provide macroscopic perspective for further mechanism research and reference for hazards mitigation of similar scenario in future. In the light of this, plenty of professionals and scholars have carried out abundant researches on coseismic landslides distribution analysis (e.g., Harp and Jibson 1996; Fukuoka et al. 1997; Keefer 2002; Wang et al. 2002; Khazai and Sitar 2003; Chigira and Yagi 2006; Wang et al. 2007; Meunier et al. 2008; Yin et al. 2009; Zhang et al. 2010; Qi et al. 2010; Dai et al. 2011; Xu et al. 2011; Gorum et al. 2011; Collins et al. 2012; Zhang et al. 2013; Papathanassiou et al. 2013; Xu et al. 2014; Guo et al. 2015; Gnyawali et al. 2016; Xu et al. 2018).

These works presented the characteristics (distribution, size and controlling factors) of the coseismic landslides under different seismic motions and different geological conditions. However, few of these studies are related to the coseismic landslides that occurred in pyroclastic fall deposits. The ternary “clay-volcanic ash-pumice” structure of the pyroclastic fall deposits determines the permeability difference, which is prone to instability under strong seismic loading and heavy rainfall infiltration. Thus, spatial distribution and controlling factors of coseismic landslides occurred in pyroclastic fall deposits should be well studied.

1.1.2 Three-dimensional slope stability analysis

Slope stability assessment on a regional scale represents a vital aspect of geoenvironmental disaster prevention and mitigation, and has been commonly utilized in slope stability analysis especially during critical rainfall events. Dozens of infinite slope analysis approaches and models (one-dimensional or two-dimensional), such as the Shallow Landsliding Stability Model (SHALSTAB, Montgomery and Dietrich 1994), the distributed Shallow Landslide Analysis Model (dSLAM, Wu and Sidle 1995), the Stability Index Mapping (SINMAP, Pack et al. 1998), the Transient Rainfall Infiltration and the Grid-Based Regional Slope-Stability Model (TRIGRS, Baum et al. 2002), have been proposed and applied in previous researches on the basis of the limit equilibrium theory. These models have advances in assessing slope stability under intense rainfall, as they incorporate the variation of groundwater table or soil moisture in response to rainfall. However, one-dimensional or two-dimensional models can not consider the three-dimensional variations of topography and soil conditions in actual slopes and commonly cause conservative computation results (Cavoundis 1987; Duncan 1996).

One challenge in slope stability analysis is how to locate the potential sliding surface. Scoops3D, developed by the U.S. Geological Survey, can regionally evaluate three-dimensional slope stability throughout the digital elevation model (DEM) utilizing 3D method of columns approach (Reid et al. 2015). Scoops3D allows the user to define a series of horizontally and vertically extended points (centers the spheres) and a certain radius increment. Then the spherical surfaces intersected by the spheres and the DEM will serve as the potential sliding surfaces, and the stability of each potential landslides encompassing many DEM cells will be computed. In addition to incorporate complex topography and 3D distributions of subsurface material parameters, Scoops3D can also include the effect of earthquakes by applying a horizontal seismic loading to the potential sliding mass in a pseudo-static analysis (Reid et al. 2015). Moreover, the wide application of Geographic Information Systems (GIS) and the availability of Digital Elevation Model (DEM) have significantly facilitated the application of Scoops3D in the assessment of slope stability on a regional scale.

Scoops3D was applied for stability analysis of various aspects and areas in previous studies. It has been employed to evaluate the stability of volcano edifices (Vallance et al. 1998; Reid et al. 2001; Vallance et al. 2004; Reid et al. 2010), coastal bluffs (Brien and Reid 2007) and loess slopes (Xin et al. 2018). Tran et al. (2018) utilized Scoops3D and TRIGRS to predict rainfall-induced landslides. Liu et al. (2018) used Scoops3D to evaluate regional slope stability considering variation of water level in reservoir. While Scoops3D has been validated to be an effective way for slope stability analysis and landslide prediction especially in response to rainfall infiltration in previous studies, it has not been applied to slope stability assessment in pyroclastic fall deposits under seismic loading yet.

The 2018 Hokkaido Eastern Iburi earthquake (Mj 6.7, Mw 6.6), which occurred on the 6th of September 2018, triggered thousands of landslides in pyroclastic fall deposits. The triggered landslides caused destructive damages to the structures and resulted in serious causalities. Hundreds of earthquakes persisted after the mainshock and there is a high possibility that the Iburi region will suffer major earthquake hitherto. An effective method to assess the seismic slope stability is of great importance for the disaster prevention and mitigation in the Iburi region. The aim of this work is to utilize the Scoops3D software to conduct a slope stability analysis of on selected sites in the Atsuma, Hokkaido, where a large number of destructive landslides occurred during the Iburi earthquake. The high-resolution DEM (5×5m) was used to construct the surface topography and the isopachs of pyroclastic fall deposits were used to construct the subsurface structures. Then a series of horizontal pseudo-acceleration coefficient proposed in previous literatures were selected to compute the slope stability under seismic loading and the results of the calculation were validated based on the landslides triggered by the Iburi earthquake.

1.2 Earthquake-triggered landslides in Japan

Japan is located in one of the most tectonically active regions in the world due to the subductions of Philippine Sea Plate and Pacific Plate to the Eurasian plates and the convergence between the North American and Eurasian Plates (Fig. 1.1). These tectonic movements resulted large numbers of earthquakes. Japan accounts for about 20% of the earthquakes of magnitude 6 or greater on the Richter scale. Each day about 1,000 tremors that can be felt are produced in Japan. More than 130,000 quakes were logged in Japan in 2005 (Hays 2010). The frequently occurred earthquakes can triggere large amounts of landslides and pose serious threats to humanity and the society.

Table 1.1 Several catastrophic earthquakes and triggered landslides in Japan in the 21st century

Earthquake	Date (JST)	Magnit	Triggered landslides
Iburi earthquake	6 Sep. 2018	Mj 6.7	5,625
Kumamoto earthquake	16 Apr. 2016	Mj 7.3	3,467 (Xu et al. 2018)
Tohoku earthquake	11 Mar. 2011	Mw	3,477 (Wartman et al. 2013)
Iwate-Miyagi earthquake	14 Jun. 2008	Mj 7.2	4,161 (Yagi et al. 2009)
Niigata Chuetsu–Oki earthquake	16 Jul. 2007	Mw 6.6	>100 (Gratchev and Towhata 2011)
Mid Niigata Earthquake	23 Oct. 2004	Mw 6.6	1,353 (Sato et al. 2005)

As is listed in Table 1.1, these catastrophic earthquakes triggered thousands of coseismic landslides. The Iburi earthquake triggered more landslides than those induced by other earthquakes (Table 1.1), thought the magnitude is smaller than other earthquake. Thus, it is of great importance to study the factors controlling the occurrence and distribution of the Iburi landslides.

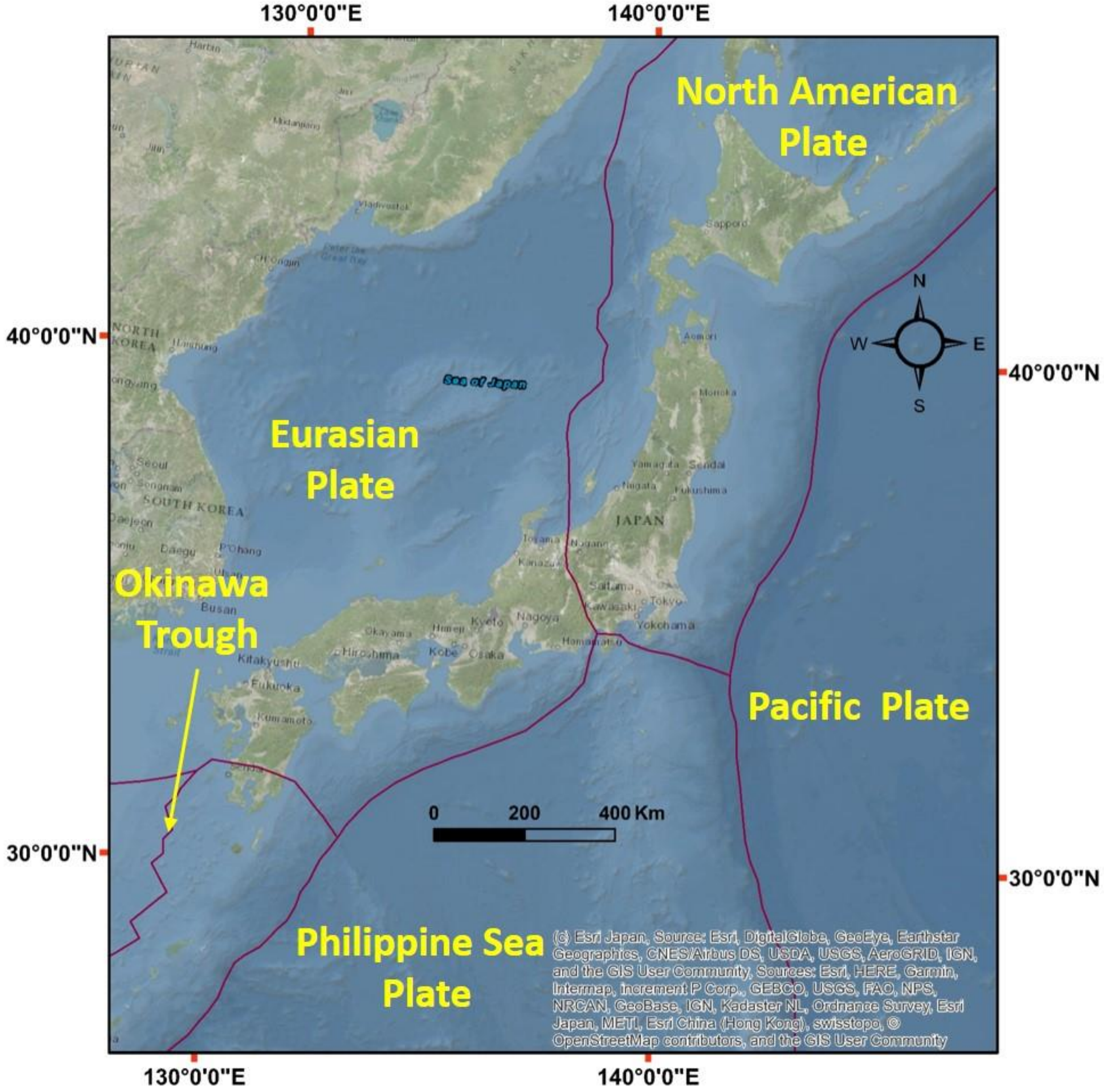

(c) Esri Japan, Source: Esri, DigitalGlobe, GeoEye, Earthstar Geographics, CNES/Airbus DS, USDA, USGS, AeroGRID, IGN, and the GIS User Community, Sources: Esri, HERE, Garmin, Intermap, increment P Corp., GEBCO, USGS, FAO, NPS, NRCAN, GeoBase, IGN, Kadaster NL, Ordnance Survey, Esri Japan, METI, Esri China (Hong Kong), swisstopo, © OpenStreetMap contributors, and the GIS User Community

Fig. 1.1 Tectonic settings around Japan

1.3 Objective and scope

This research aims to understand the distribution and failure mechanism of the shallow landslides triggered by the Iburi earthquake and assess the seismic slope stability on a regional scale.

The major objectives of the research projective are as follows:

(1) To delineate a detailed and comprehensive landslide inventory map covering all the slope failures resulted from the Iburi earthquake;
(2) To analyze the general distribution trend of the coseismic landslides;
(3) To classify the types, size characterization of the Iburi landslides and to study the failure mode of the Iburi landslides;
(4) To explore the factors controlling the occurrence and distribution of the slope failures triggered by the Iburi earthquake;
(5) To assess the seismic slope stability on a regional scale and to select a horizontal pseudo-acceleration coefficient range suitable for seismic slope stability analysis in pyroclastic fall deposits.

In addition, the occurrence of coseimic landslides in the old landslide areas (slope failures occurred before the Iburi earthquake) is also studied, and the relatively high occurrence of coseimic landslides in the old landslide areas is also explained.

1.4 Thesis structure

This thesis is focused on the theme of understanding the distribution and controlling factors of the Iburi landslides, as well as three-dimensional seismic slope stability assessment in the Iburi regions.

Chapter 1 reviews previous research on the earthquake-triggered landslides and three-dimensional slope stability assessment.

Chapter 2 describes the Iburi earthquake and the geological conditions as well as preceding rainfall conditions in the affected region.

Chapter 3 presents characteristics of the Iburi landslides based on a complete landslide inventory including general spatial distribution, landslide types, possible failure, size characteristic, and slope failures in old landsliding areas.

Chapter 4 analyzes the effect of the controlling factors on the occurrence and distribution of the slope failures resulted from the Iburi earthquake.

Chapter 5 utilizes a Fortran program, Scoops3D, to assess the seismic slope stability on a regional scale on a severely destructed area in Atusma, Hokkaido.

Chapter 6 concludes the thesis by highlighting several findings of the Iburi landslides and a horizontal pseudo-acceleration coefficient range suitable for seismic slope stability analysis in pyroclastic fall deposits is proposed.

CHAPTER 2

IBURI EARTHQUAKE AND COSEISMIC LANDSLIDES

2.1 Iburi earthquake

The 2018 Iburi earthquake occurred at 03:07:59.3 am (JST) on the 6th of September 2018 (18:07:59.3 UTC of September 5th) in the eastern and central Iburi regions of Hokkaido, Northern Japan, one-day after the passage of Typhoon Jebi (Typhoon No. 21) through this area. The epicenter of the Mj 6.7 (Mw 6.6) mainshock (N 42°41.4′, E 142°00.4′, JMA; N 42.686°, E 141.929°, USGS) was located at Atsuma, Hokkaido approximately 300 km away from the southeastern Kuril Trench. The maximum seismic intensity was 7.0 according to the Japan Meteorological Agency (JMA) seismic intensity scale, corresponding to approximately X on the Modified Mercalli Intensity (MMI) scale. The focal mechanism of the mainshock (with a focal depth of about 37 km) was inferred as being a high-angle reverse fault type with an ENE-WSW compression axis (according to the Headquarters for Earthquake Research Promotion, Japan). During the earthquake, 41 people were killed and 691 people were injured; 394 houses were completely destroyed and 1,061 houses were damaged (based on reports by the Ministry of Internal affairs and Communications, Japan). Even though the regional seismicity attenuated thereafter, a sequence of persistent aftershocks occurred. Three hundred and eleven aftershocks with a maximum seismic intensity larger than 1.0 were reported by JMA up to the 31st of October 2018 (Fig. 2.1). Most aftershocks were concentrated in a rectangle with NS length of 30 km and EW width of 5 km (Fig. 2.2).

The electric power facilities in the afflicted region were greatly damaged by the strong seismic shaking. The largest thermal electric power plant in Hokkaido, Tomato-Atsuma Station, is located 18 km away east-southeast from the epicenter (Takahashi and Kimura 2019). Multiple consecutive factors such as the shutdown of the Tomato-Atsuma electric power plant, and the shutdown of the hydroelectric power plants due to trouble in electric power lines, led to the long-term blackout in the whole Hokkaido area of 2,950,000 houses at 03:25 on September 6, 2018, 18 minutes after the mainshock (Cabinet office 2018; Organization for Cross-regional Coordination of Transmission Operation, Japan 2018). Emergency generators were activated at the Tomari nuclear power plant because of the loss of external electric power (Cabinet office 2018). The electric power loss in Hokkaido caused severe damage to its livelihood and economic activities. Though the recovery time varied from place to place, it was not restored till September 8 (Hokkaido Prefectural Government 2018). Several seismic stations were operated with the help of emergency batteries (Japan Meteorological Agency). The recovery time of the Institute of Seismology and Volcanology of Faculty of Science, Hokkaido University was at 14:00 on September 8 (Takahashi and Kimura 2019).

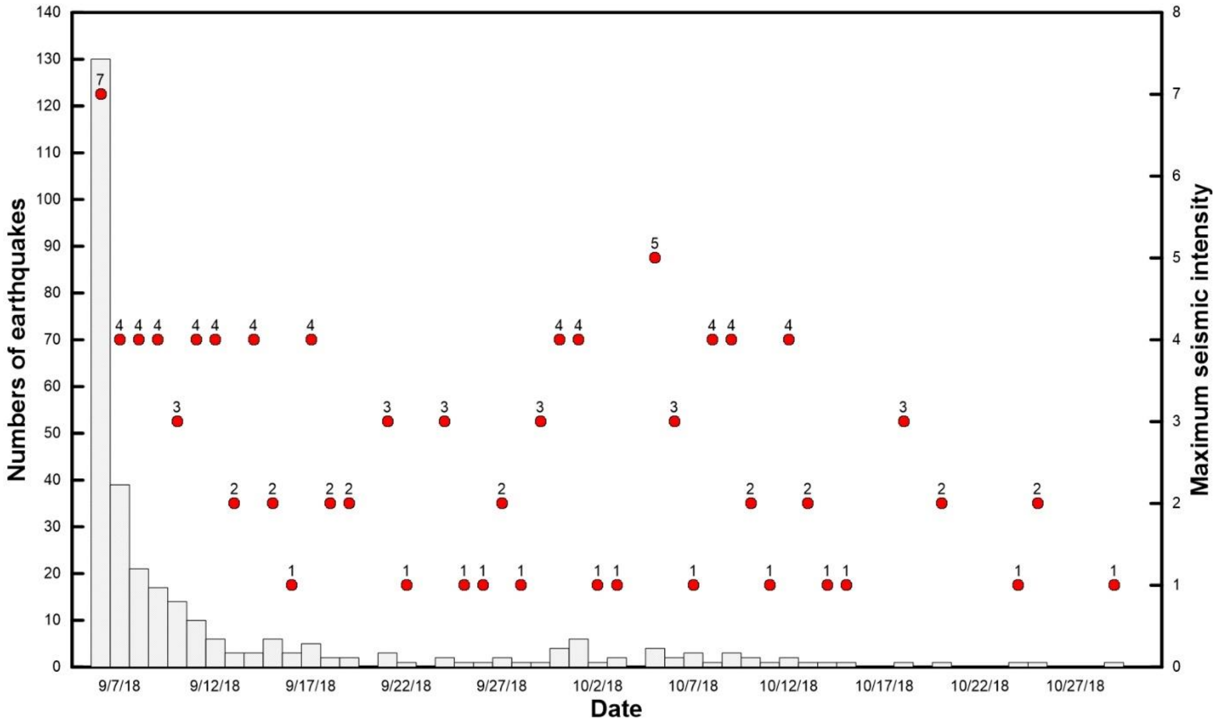

Fig. 2.1 Earthquakes with a maximum seismic intensity larger than 1.0 during 6th of September to the 31st of October 2018 (announced by JMA)

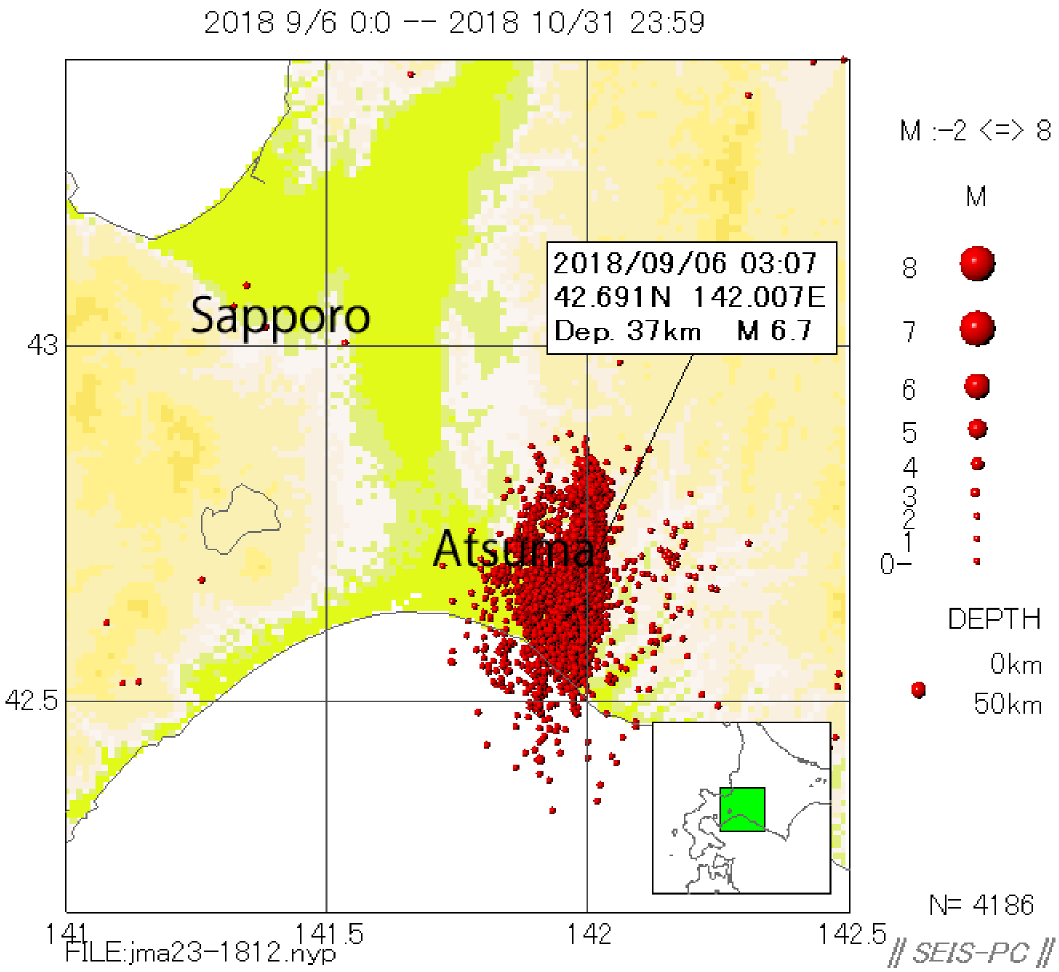

Fig. 2.2. Mainshock and aftershock epicenters from September 6 to October 31, 2018 (Takahashi and Kimura 2019)

Intense ground motion and shaking were generated and serious damage was inflicted in the severely affected areas during the earthquake. Numerous secondary geo-disasters including landslides, liquefaction, and valley damming by landslides occurred in Atsuma and the adjacent areas. The coseismic landslides resulted in 36 casualties (Yamagishi and Yamazaki 2018). The disaster was the cause of significant concern and received much attention in Japan and the rest of the world. Disaster relief operations and preliminary field investigations were conducted by relevant institutes, organizations, and the Japanese government immediately after the earthquake. A landslide database including 3,307 sites was published thereafter by the Geospatial Information

Authority of Japan. A further interpretation based on high-resolution aerial images, valley lines, ridge lines, hillshade, and slope aspect generated by the 10 m resolution digital elevation model (DEM) was conducted in this work. As a result, 5,625 coseismic landslides covering an area of 46.3 km^2 were identified (Fig. 2.3). Most of the landslides are translational landslides with small scars and shallow-sliding surfaces and moved for long run-out distance, showing high mobility. Only one deep-seated landslide was identified.

Two hypotheses have been proposed to explain the numerous landslides observed in the HEIE earthquake (Wang et al. 2019). The first hypothesis suggests that the extensive rainfall in the previous day due to typhoon Jebi could have led to saturation of pumice strata (Petley 2018), which is one of the most widespread geomaterials on the slopes in Iburi and its surrounding areas, and known to absorb large quantities of water. Hence, it may have caused a rapid pore-pressure increase in the surficial soils during ground shaking and led to liquefaction and slope failure (Wang et al. 2019). The second hypothesis highlights that the unprecedented strong motion was the key factor for the coseismic landsliding (Normile 2018).

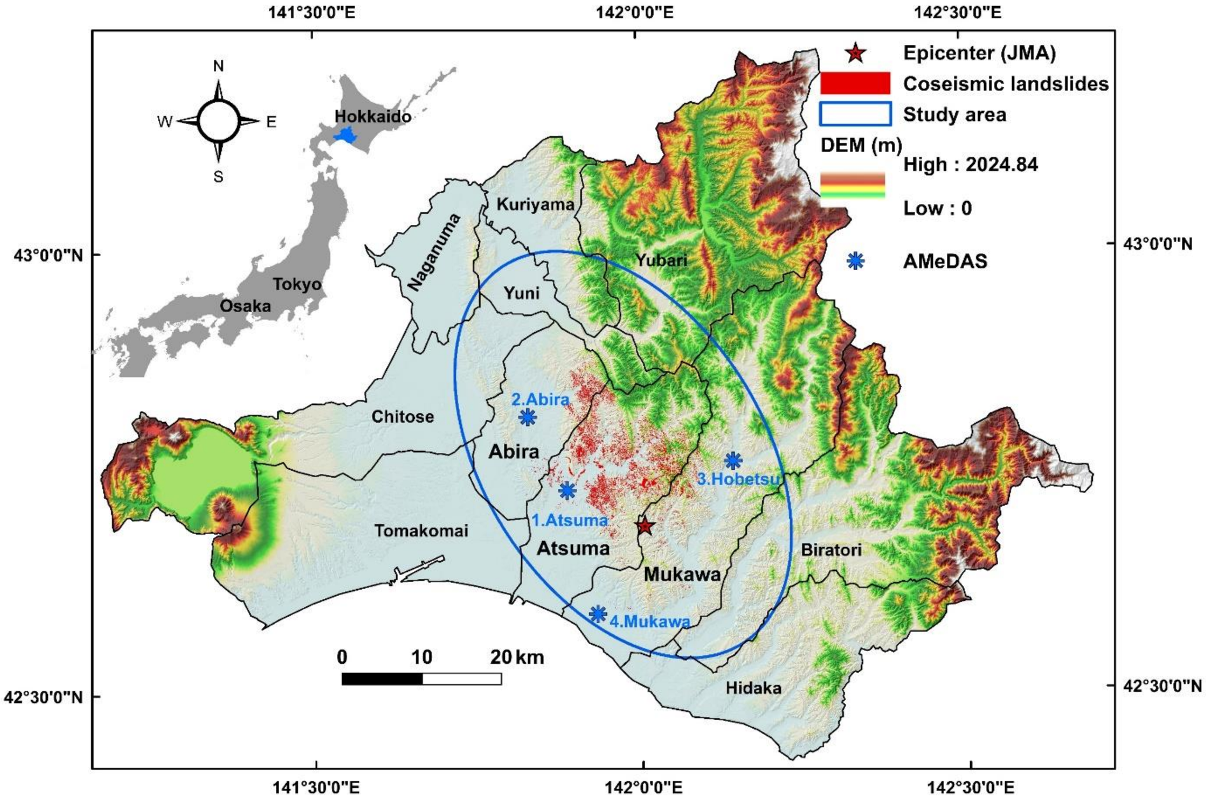

Fig. 2.3 Location map and coseismic landslide distribution map

2.2 Geological setting

Hokkaido is located in one of the most tectonically active regions in the world. It is subjected to westward subduction of the Pacific Plate and convergence between the North American and Eurasian Plates (Kimura 1994; Tamaki et al. 2010). More specifically, due to the collision of the Northeast Honshu Arc-Japan Trench and the Kuril Arc-Trench, Hokkaido presents complex tectonic associations and geological features (Arita et al. 1998). Numerous earthquakes have occurred along the southwestern region of the Kuril Trench, such as the 1993 Mw 7.6 Kushiro-Oki earthquake, the 1994 MJMA 8.1 Hokkaido-Toho-Oki earthquake, and the 2003 Mw 8.3 Tokachi-Oki earthquake (Arita et al. 1998; Okamura et al. 2008). The Hidaka Collision Zone, which is an area of deformation characterized by right-lateral strike-slip movement in central Hokkaido, consists of five belts, i.e., the Sorachi-Yezo Belt (SY), the Idonnappu Belt (ID), the

Hidaka Belt (HD), the Yubetsu Belt (YB) and the Tokoro Belt (TB) (Fig. 2.4) (Kimura 1983). Their ages range from the Late Jurassic to Paleogene (Kimura 1983).

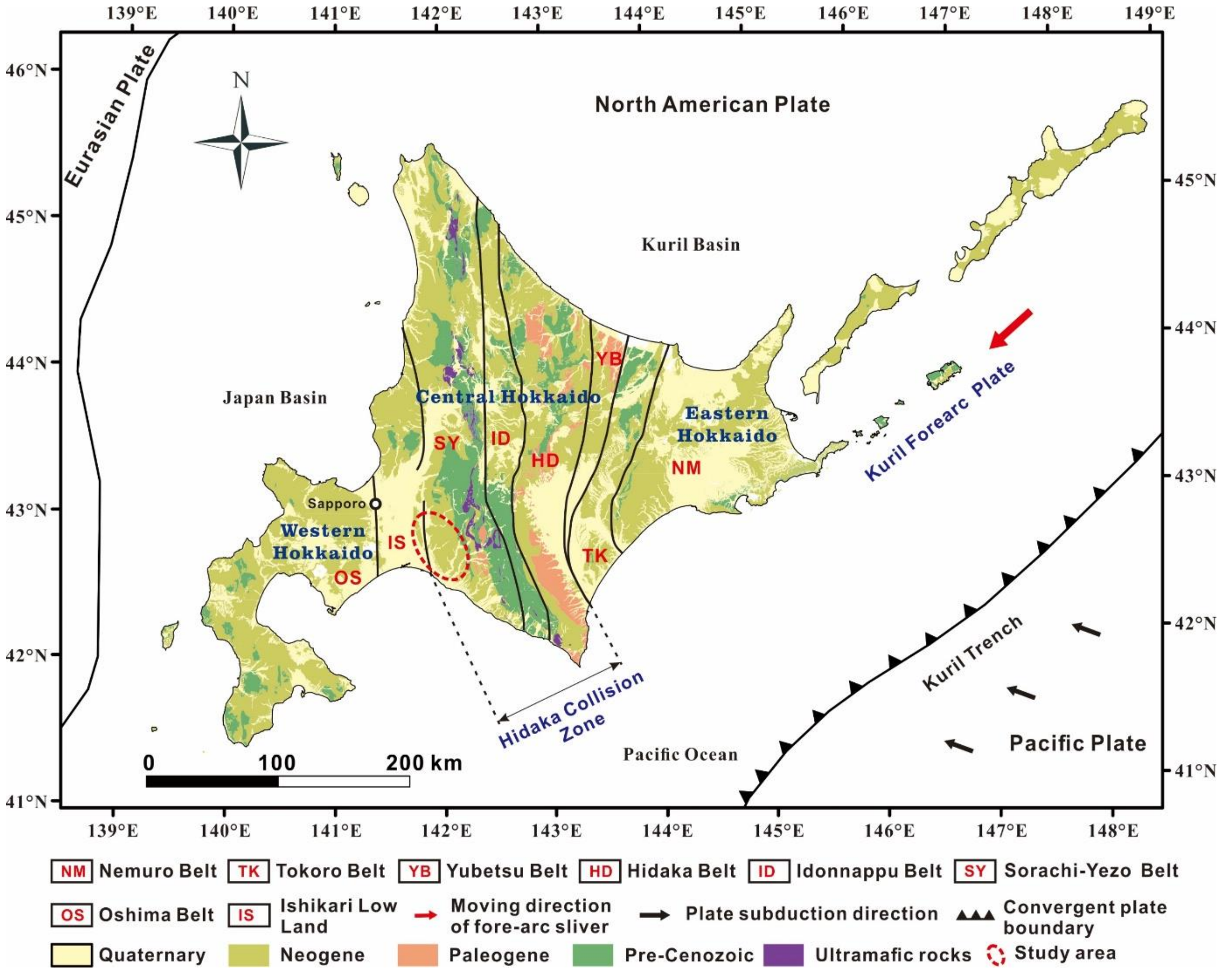

Fig. 2.4 Simplified tectonic setting and geochronology around Hokkaido. Tectonic divisions are modified after Kimura (1994), Arita et al. (1998) and Takashima et al. (2002). Plates boundaries are derived from U.S. Geological Survey. Geochronologic map is classified based on 1:200,000 geological map of Japan from Geological Survey of Japan, AIST

The study area is situated at the frontal fold and thrust belt created by the westward vergence of the Hidaka Mountains (Ozaki and Taku 2014) and extending to an adjoining lowland terrace

(Ishikari Depression). Faults and active faults in this region are extremely developed with near north-south strikes, especially at the Eastern Boundary Fault Zone of the Ishikari Lowland (Fig. 2.5). The main part of the Eastern Boundary Fault Zone of the Ishikari Lowland originates from Bibai and ends at Abira, Yufutsu with a convex curve distribution striking from NNE/SSW to NNW/SSE. Two reverse active fault zones (behavioral segments) of the Eastern Boundary Fault Zone of the Ishikari Lowland (i.e., the Yufutsu faults and the Maoi faults) run across the study area. Another active fault, the Karumai behavioral segment, is located southwest to the epicenter of the Iburi earthquake (Fig. 2.5). Two major faults, the Atsuma fault and Biratori fault, with a general NNW/SSE trend, are in the central study area. Eighteen geological units (including water) were classified based on a 1:200,000 seamless geological map and the Seamless Geoinformation of Coastal Zone “Southern Coastal Zone of the Ishikari Depression” (Ozaki and Taku 2014) published by the Geological Survey of Japan, AIST. The bedrock strata in the area are dominated by Neogene and Quaternary marine and non-marine sedimentary rocks and Late Pleistocene non-alkaline pyroclastic flow volcanic rocks (Ozaki and Taku 2014). The eastern part is characterized by rugged terrain along with high elevations and presents complex lithologic characteristics. The main strata of the eastern area are represented by Eocene to Oligocene coal-bearing fluvial and marine sedimentary rocks, Early Miocene to Middle Miocene mudstone, sandstone, and alternating beds of sandstone and mudstone with conglomerate and tuff, and Late Cretaceous marine muddy turbidite and mudstone. In addition, ultramafic rocks and Early to Middle Miocene mafic plutonic rocks (which may indicate complex tectonic movement) are also scattered in the vicinity. The hilly central study area is underlain by Middle Miocene to Pliocene mudstone, siltstone, sandstone, and conglomerate. The western part is located in the Ishikari Low Land and consists of Late Pleistocene to Holocene fluvial deposits and Late Pleistocene non-alkaline pyroclastic flow volcanic rocks.

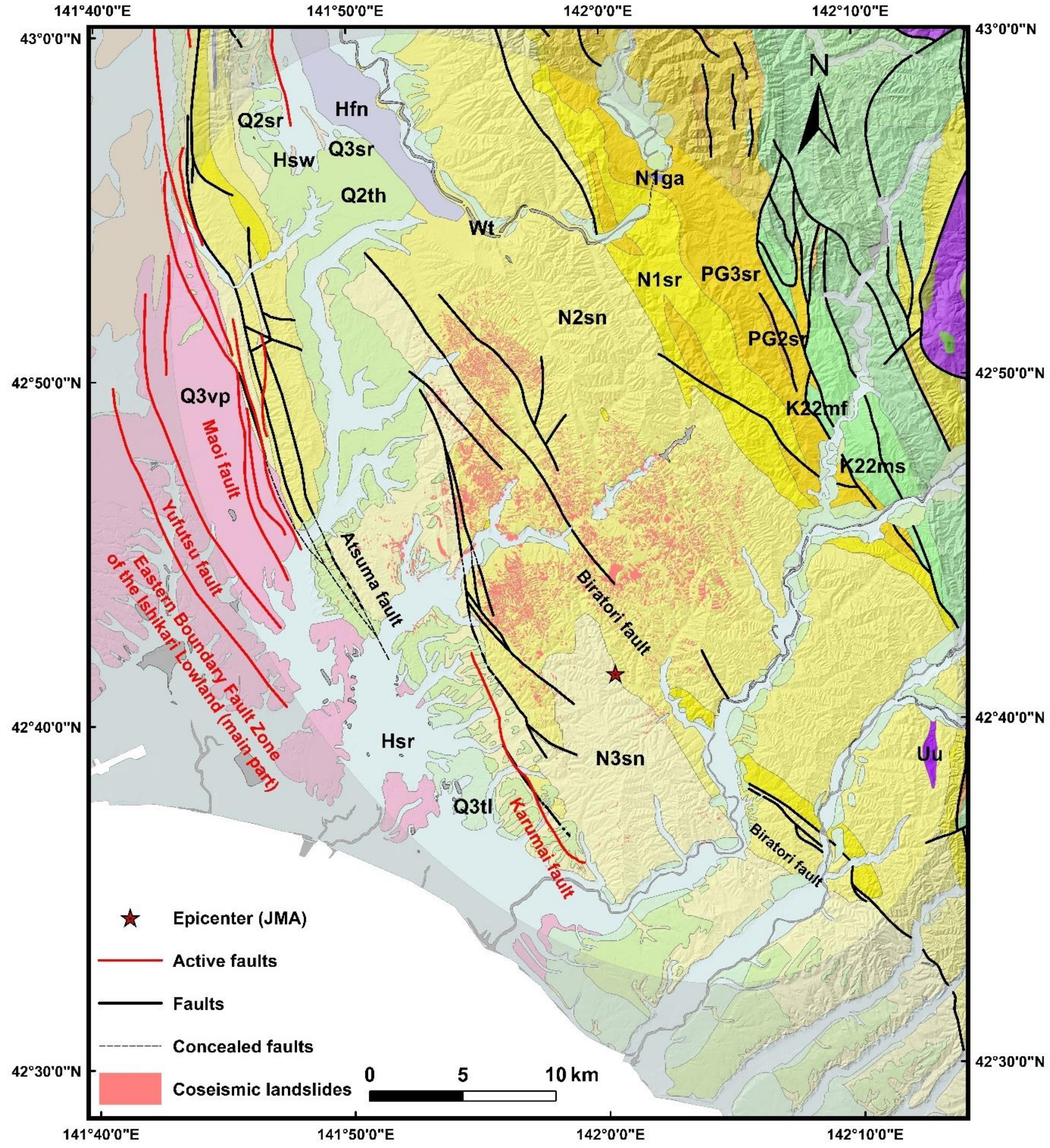

Fig. 2.5 Geological setting of the study area. Geological units and (active) faults are categorized based on the 1:200,000 seamless geological map published by the Geological Survey of Japan, AIST. The descriptions of geological units (such as N2sn, Hsr, Q3tl, and Q3vp) are listed in Table 2.1

Table 2.1 Classification of geological units and coseismic landslides occurred in each unit

Code	**Age**	**Lithology**	**CA (km^2)**	**LSN**	**LSA**
N2sn	Middle to Late Miocene	Sandstone, mudstone, conglomerate and sandstone (with tuff)	**606.3**	**4,924**	**41.7**
N3sn	Late Miocene to Pliocene	Diatomaceous siltstone with sandstone and conglomerate	**199.1**	**517**	**3.1**
Hsr	Late Pleistocene to	Clay, silt, sand, gravel and peat	**230.4**	**88**	**1.1**
Q2th	Middle Pleistocene	Mud, sand, gravel and peat	**129.2**	40	0.1
N1sr	Early Miocene to Middle	Mudstone, sandstone and conglomerate (with tuff)	82.7	20	0.1
Q2sr	Middle Pleistocene	Mud, sand, gravel and peat	17.1	23	0.2
Q3tl	Late Pleistocene	Mud, sand, gravel, peat and volcanic materials	53.5	8	0.1
PG3sr	Late Eocene to Early	Tuffaceous siltstone with sandstone and conglomerate	79.3	2	0.002
Q3sr	Late Pleistocene	Sand and volcanic ash sand	0.1	0	0
Hsw	Late Pleistocene to	Swamp deposits	0.9	0	0
PG2sr	Middle Eocene	Sandstone, mudstone and conglomerate (with coal and tuff)	1.0	0	0
N1ga	Early to Middle Miocene	Basaltic andesite	0.3	0	0
K22mf	Late Late Cretaceous	Marine muddy turbidite	4.8	0	0
Q3vp	Late Pleistocene	Rhyolite pumice block, lapilli and ash	84.0	0	0
Hfn	Late Pleistocene to	Fan deposits gravel, sand and mud (with peat and volcanic ash)	21.8	0	0
Uu	Unknown	Ultramafic rocks	1.8	0	0
K22ms	Late Cretaceous	Marine sandstone	32.3	0	0
Wt		Water	12.5	3	0.04
Total			1,557.2	5,625	46.3

CA (class area) is the area of each class; LSN (landslide number) is the number of landslides in each class; LSA (landslide area) is the area of landslides occurred in each class. The bold numbers in the column of "CA" denote areas of four classes larger than 100 km^2; the bold numbers in the "LSN" and "LSA" columns represent the largest three values of corresponding classes

It is very important to note that surface soil layers in the study area are composed of pyroclastic tephra deposits mainly derived from mounts Tarumae and Eniwa. At least three cyclothemic interbedded layers, i.e., Tarumae-d pyroclastic fall deposits, Tarumae-c pyroclastic fall deposits and Tarumae-a, b pyroclastic fall deposits were determined (Tajika et al. 2016). The nethermost layer comprised paleosol (Ta-d loam) and Tarumae-d pyroclastic fall deposits (8 to 9 ka), including lithic fragments (Ta-d1) and pumice fall (Ta-d2). Middle humus and Tarumae-c pyroclastic fall deposits (2.5 to 3 ka) constituted the second layer. Humic surface soil, Tarumae-a pyroclastic fall deposits and Tarumae-b pyroclastic fall deposits at the top made up the surface layer (Tajika et al. 2016). The total depth of the pyroclastic tephra deposits distributed in the study area above is approximately 4 to 5 m (Yamagishi and Yamazaki 2018).

2.3 Preceding rainfall

The Iburi earthquake occurred only one day after the passage of the Typhoon Jebi (Typhoon No. 21). The Iburi region is considered to have experienced torrential rainfall during the destructive typhoon. Based on rainfall data delivered by Japan Meteorological Agency, daily and cumulative precipitation of four available AMeDAS stations (Fig. 2.3) during the period of 6 August 2018 to 11 September 2018 are depicted in Fig. 2.6. In contrast to widespread opinion, the cumulative rainfall from 1 to 5 September is surprisingly less than 20 mm for all four AMeDAS stations (Fig. 2.6). The low precipitation brought by Typhoon Jebi is unlikely to cause the high saturation of surface soil observed in the field. Figure 4 illustrates that the study area experienced prolonged rainfall in August, especially during the period from 13 August to 17 August. The cumulative rainfall recorded by the four stations in this period is between 101 mm and 120 mm. Persistent rainfall in August may greatly contribute to the occurrence of landslides during the intense ground shaking of Iburi earthquake.

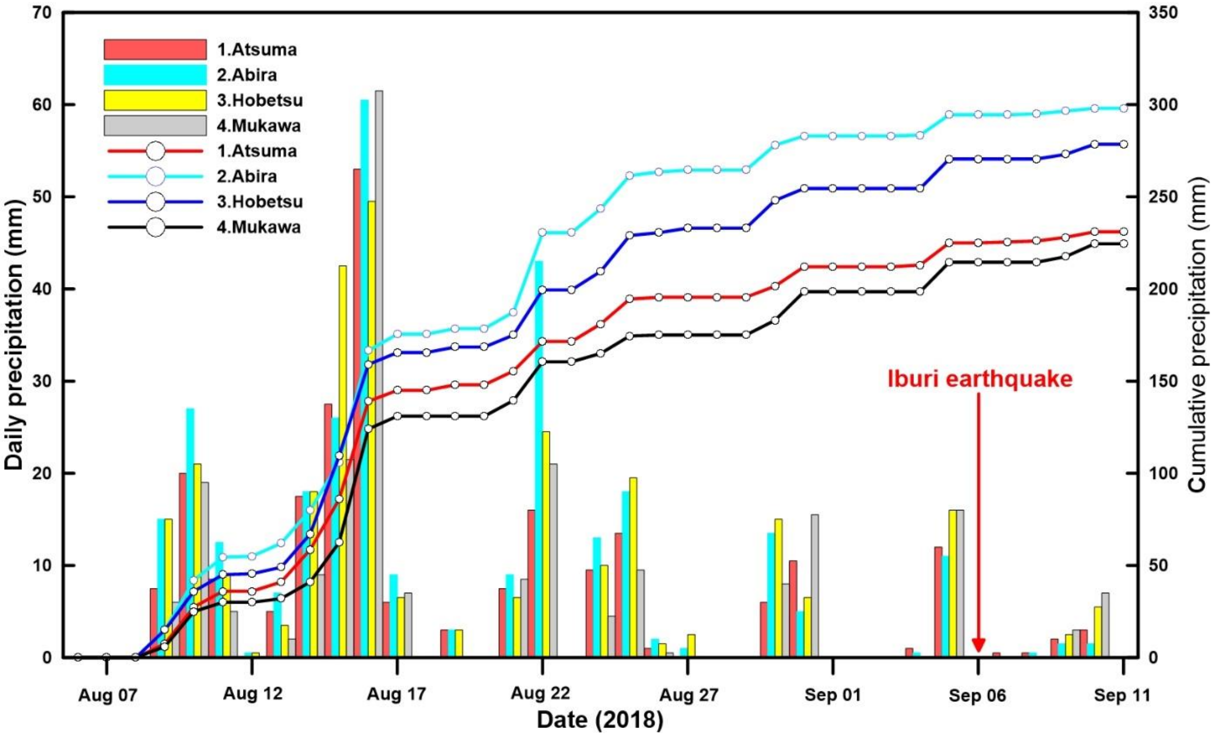

Fig. 2.6 Daily and cumulative precipitation from 6 August 2018 to 11 September 2018

CHAPTER 3

CHARACTERISTICS OF THE IBURI LANDSLIDES

3.1 Landslide inventory

The Iburi earthquake triggered densely distributed slope failures in the vicinity of Atsuma, Mukawa, and Abira (Fig. 3.1). A first-hand database including 3,307 landslide sites was released by the Geospatial Information Authority of Japan several days after the mainshock. Most of the released landslides are composed of several or dozens of landslides. Thus, further manual segmentation and combination regarding unreasonable landslide units were carried out on the base of valley lines, ridge lines, hillshade, and slope aspect generated by the 10 m resolution DEM (as well as high-resolution aerial images). A detailed landslide inventory map incorporating 5,625 individual landslides (Fig. 3.1) and covering 46.3 km^2 was created. Most coseismic landslides occurred in the transition zone from the Hidaka Mountains towards the Ishikari Depression.

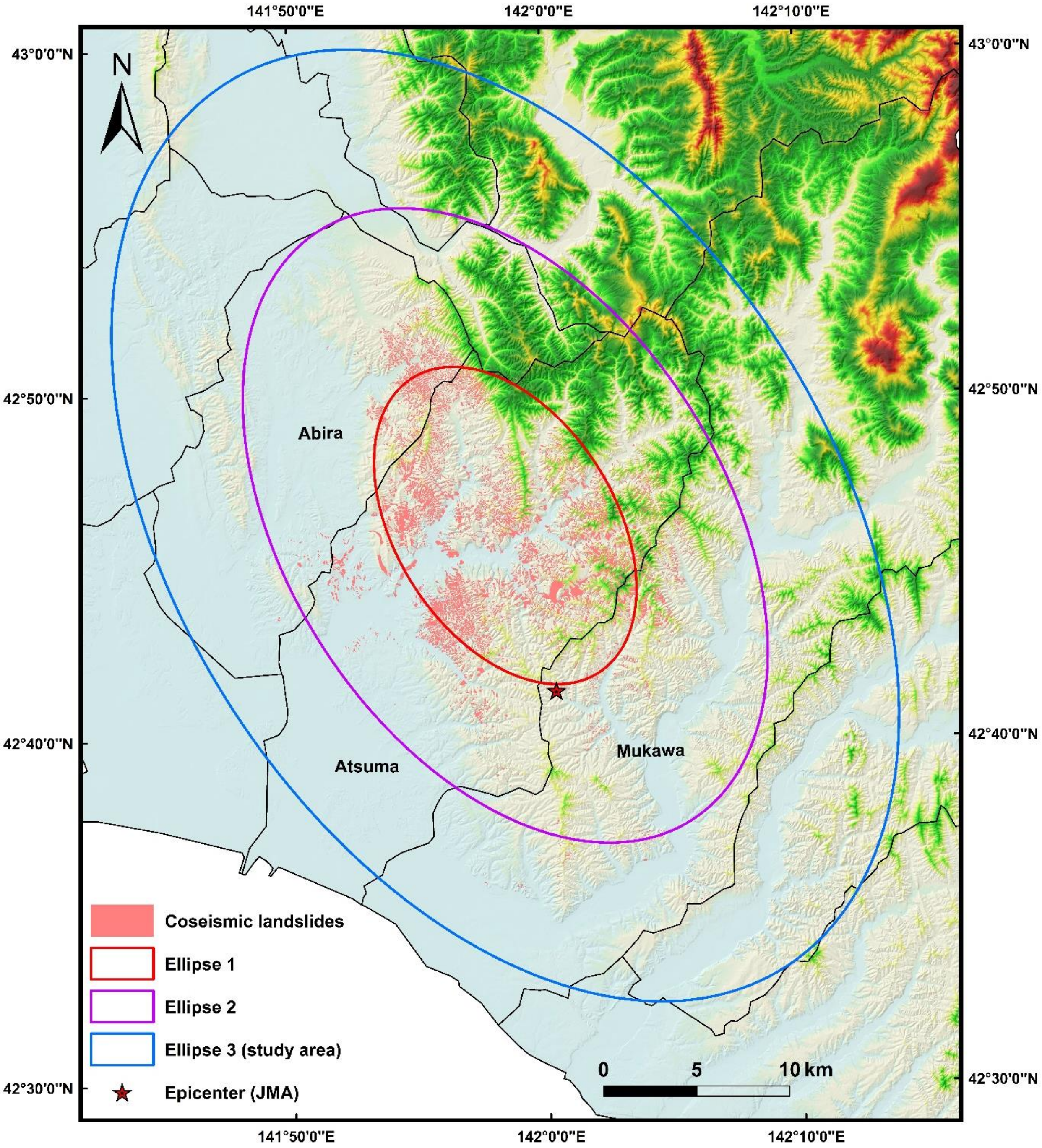

Fig. 3.1 Coseismic landslide inventory map

3.2 General spatial distribution

The spatial distribution of the coseismic landslides conveys vital information regarding the propagation and dissipation of the seismic wave, and provides basic reference for further susceptibility analysis and post-earthquake disaster mitigation and relief. The Directional Distribution Tool (Standard Deviational Ellipse) Tool in ArcGIS 10.6 can generate an ellipse with a particular orientation indicating the general trend of the features. It calculates the standard distance (standard deviation) for a set of features (points or polygons) from the mean center of the features in the x and y directions, and these measures are then used to define the axes of the ellipse (https://pro.arcgis.com/en/pro-app/tool-reference/spatial-statistics/directional-distribution.htm). Furthermore, the Directional Distribution Tool can produce three ellipses containing certain percentages of the features using different variance scaled by different adjustment factors, i.e., one standard deviation, two standard deviations, and three standard deviations (https://pro.arcgis.com/en/pro-app/tool-reference/spatial-statistics/h-how-directional-distribution-standard-deviationa.htm). It is noted in ArcGIS Help 10.6 that the generated ellipses corresponding to three standard deviations cover approximately 63%, 98% and 99.9% of the features in two dimensions.

In this work, the Directional Distribution Tool was utilized to explore the general distribution characteristics of the coseismic landslides. Three ellipses corresponding to three standard deviations were created ((Fig. 3.1), and they shared same center (N 42.770°, E 141.974°) as well as the orientations of the major and minor axes. The direction of the major axes of three ellipses (327.7°), representing the general distribution trend of the 5,625 landslides triggered by the Iburi earthquake sequence, is approximately identical to the strikes of faults and active faults in this region. These three ellipses with the coverage of 1,557 km^2, 692 km^2, and 173 km^2 encompass 5,625, 5,508 and 3,638 coseismic landslides, respectively. The LCs (landslide concentration, the ratio of landslide number and the corresponding ellipse area) of the three ellipses are as high as 21.0 per km^2, 8.0 per km^2 and 3.6 per km^2, respectively. The three ellipses definitely designate the landslide-triggered areas with different severities, which can offer the guidance for deploying disaster relief operations and mitigation strategies efficiently.

3.3 Types of coseismic landslides

A five-day on-site field reconnaissance (beginning on 10 September 2018) as well as aerial photography interpretation, indicated that most coseismic landslides were coherent shallow debris slides and disrupted mobilization of valley fill. Only one deep-seated landslide (Horonai landslide, Fig. 3.2) was recognized. The locations of three typical investigated landslides are shown in Fig. 3.2.

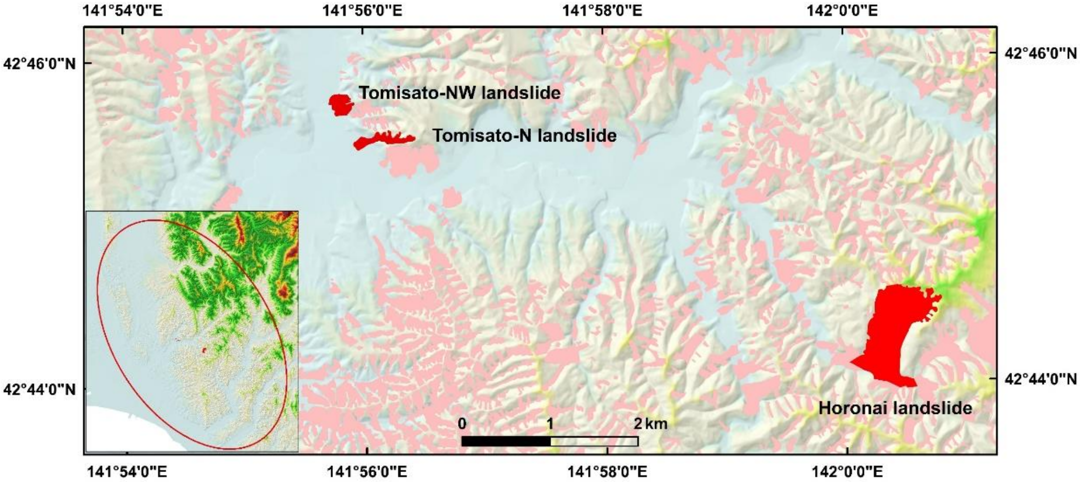

Fig. 3.2 Locations of three typical investigated landslides

The Tomisato-NW landslide (Fig. 3.3) is a typical shallow debris slide with a width of about 250 m. The slope failure initiated from the hill-top, entraining large amounts of vegetation and tephra deposits, which destroyed the farmland in the lower footslope, and came to rest at the meandering river in the middle of the farmland (Fig. 3.3a). The mobilized apparent friction angle (Sassa et al. 1996; Sassa et al. 2005) of the Tomisato-NW landslide is approximately 10.3°. Field investigation discovered that the sliding surface in the source area of the Tomisato-NW landslide is covered by approximately 0.1 m to 0.2 m thick crushed pumice (Figs. 3.3b and 3.3c). Another predominant type of coseismic landslides is the mobilization of valley fill, as represented by the Tomisato-N landslide (Fig. 3.4). The Tomisato-N landslide began from the collapse of the gully head, incorporated a vast sliding mass along the valley, heaped irregularly at the gully mouth, and ruined several houses (Figs. 3.4a, 3.4b and 3.4c). Figures 3.4d and 3.4e illustrate the soil composition of the Tomisato-N landslide in the right flank and in the scarp. The top layer has a grey-colored fine humic surface with a depth of about 300 mm (Ta-a, b in Fig. 3.4e). The middle layer is composed of middle humus and Tarumae-c pyroclastic fall deposits formed about 2,000 years ago (Ta-c in Fig. 3.4e), while the bottom layer is composed of brownish and greyish pumice (Ta-d in Fig. 3.4e). The grain size of the bottom layer decreases from the lower to upper part. The potential sliding surface is located in the greyish-green dense pumice (L7 in Figs. 3.4d and 3.4e) deposited about 9,000 years ago. The cyclothemic soil composition is closely related to the historic eruption and repose of the Tarumae Volcano (Tajika et al. 2016), and most coseismic landslides occurred in the interface between Ta-d pumice layers and the underlying paleosol. The Horonai landslide, with an area of about 0.57 km^2, is the largest landslide and the only deep-seated landslide triggered by the Iburi earthquake. The mobilized apparent friction angle of the Horonai landslide is approximately 7.1°. The sliding mass of the disrupted Horonai landslide is composed of overlying tephra deposits (volcanic ash and pumice, Fig. 3.5b) and occasionally outcropped Miocene sedimentary rocks (diatomaceous to siliceous mudstone and glauconite sandstone, Figs. 3.5c and 3.5d). The Horonai landslide is seated at the upthrown side of the Biratori reverse fault (Fig. 2.5), and encompasses three old landslides (Fig. 3.5a). The existence of the Biratori reverse fault and the three old landslides may have contributed to the occurrence of this deep-seated landslide.

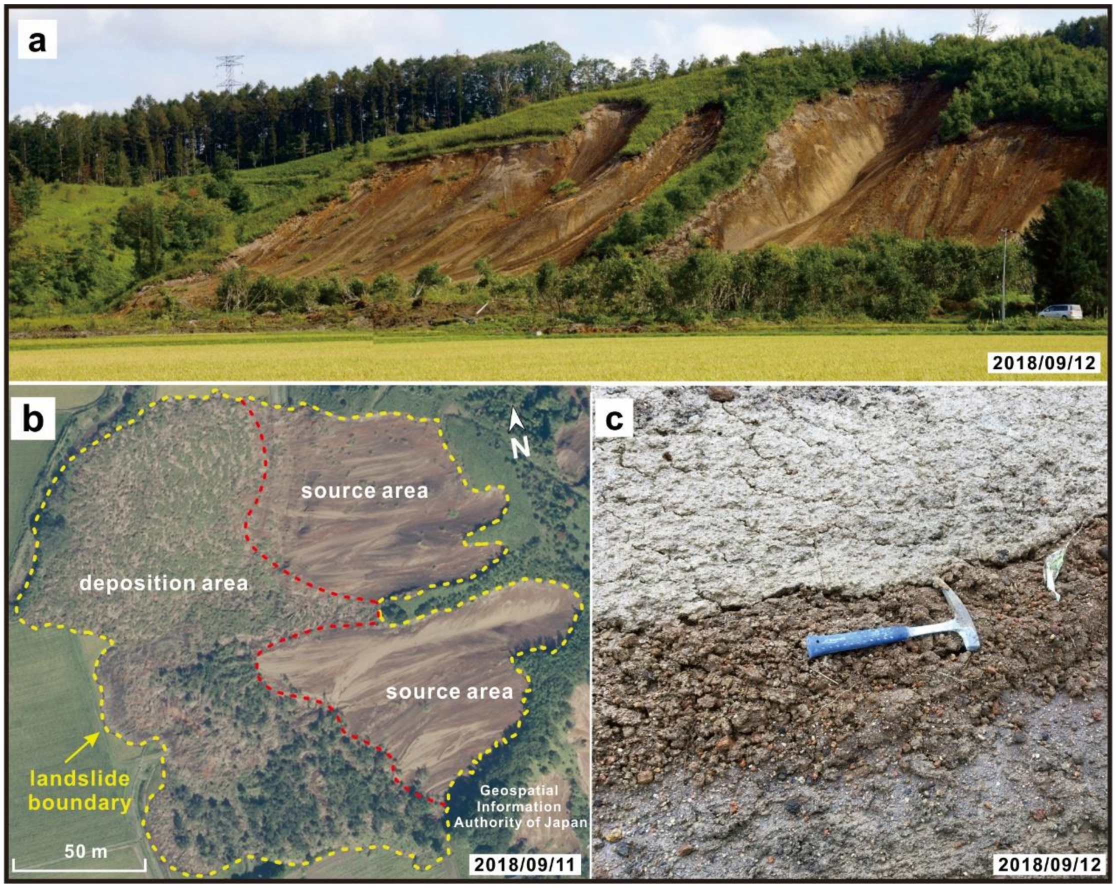

Fig. 3.3 The Tomisato-NW landslide. **a** Front panoramic view. **b** Aerial view based on Geospatial Information Authority of Japan. **c** Crushed pumice layer on the exposed sliding surface

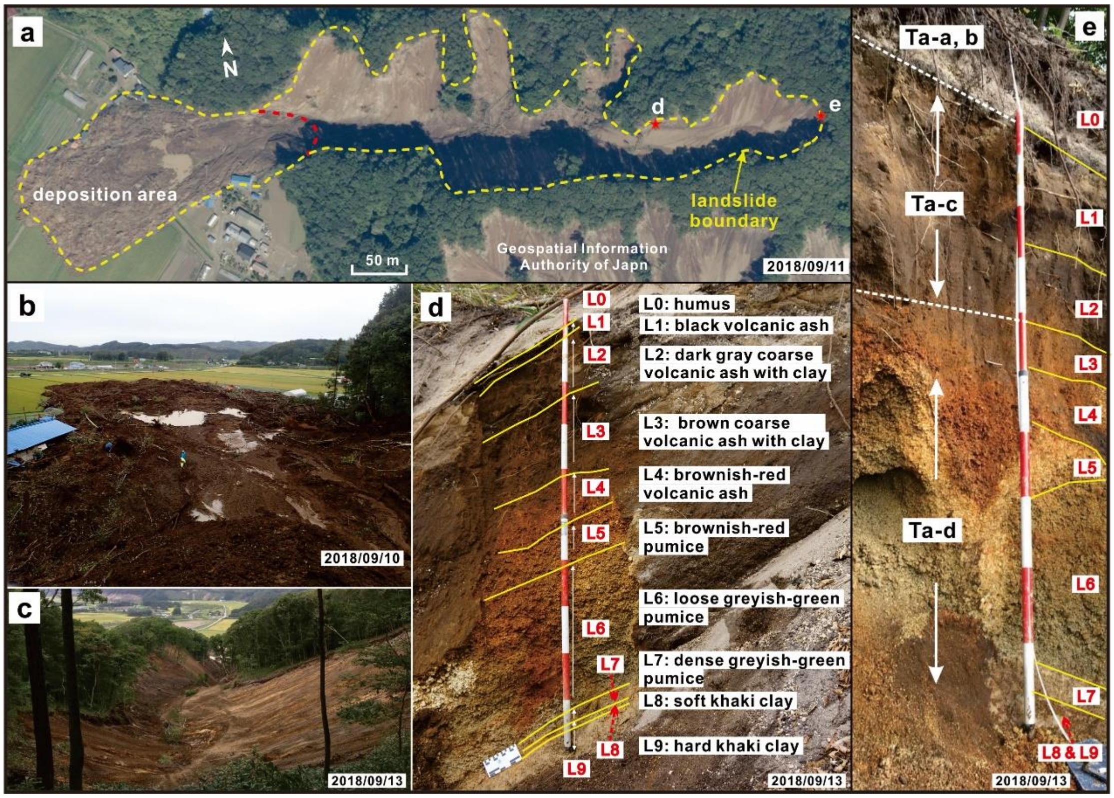

Fig. 3.4 The Tomisato-N landslide. **a** Panoramic view based on Geospatial Information Authority of Japan. **b** General view of the deposition area. **c** Valley fill. **d** Soil structure of the right flank. **e** Soil structure of the scrap

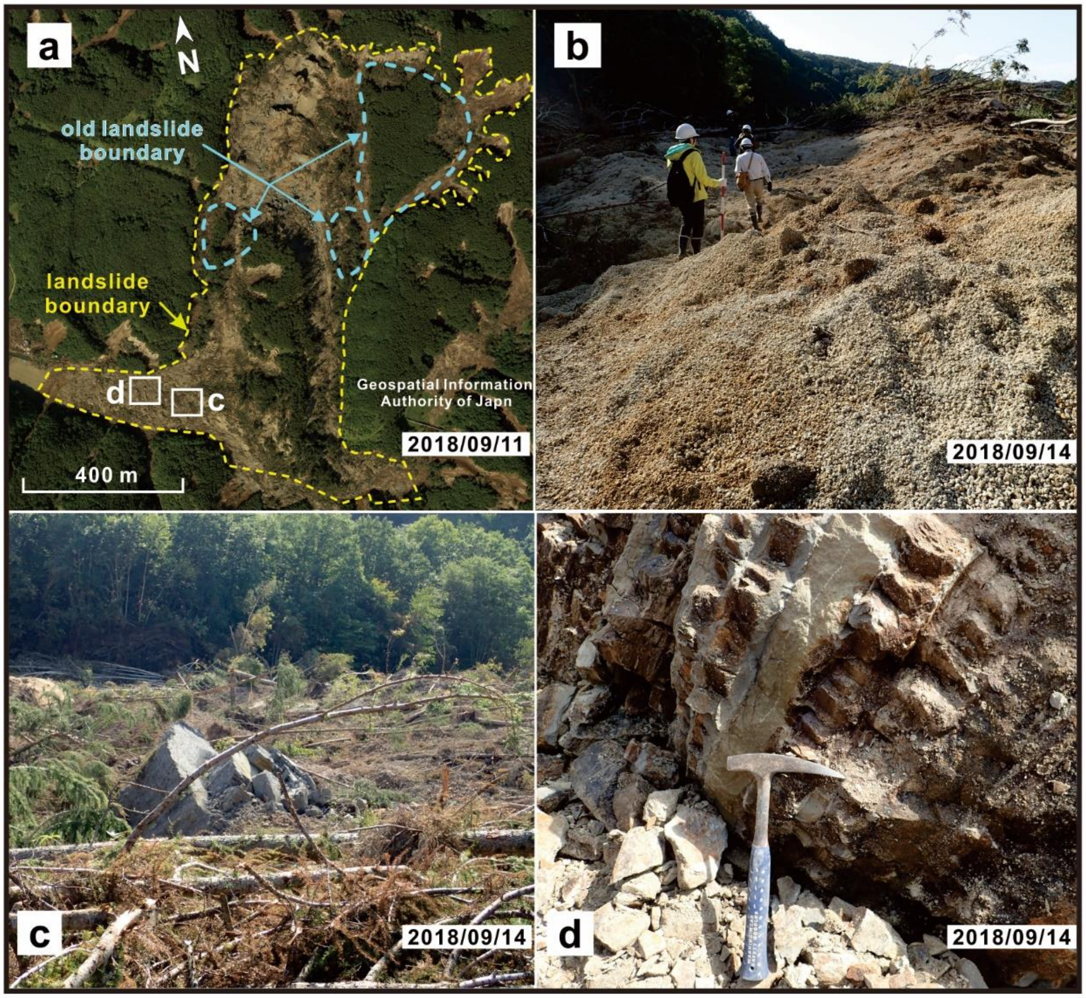

Fig. 3.5 The gigantic deep-seated Horonai landslide. **a** General aerial view based on Geospatial Information Authority of Japan. **b** Pumice on the sliding mass. **c** Disrupted sliding mass and overturned mudstone. **d** Mudstone and sandstone in the deposition area

3.4 Coseismic landslides occurred in old landsliding area

To study the relationship between the old landslides and the coseismic landslides which occurred in this event, a comparison of the 5,625 coseismic landslides that occurred in the Iburi earthquake was compared with 1,649 previous landslides derived from the 1:50,000 landslide distribution map provided by the National Research Institute for Earth Science and Disaster Resilience. The Intersect tool in ArcGIS 10.6 was used to generate 273 intersected polygons. Further manual recognition and processing revealed that these 273 intersected polygons were separately involved in 110 old and 109 coseismic landslides (Fig. 3.6). The overlapping area of the 110 old landslides and the 109 coseismic landslides is 1.2 km^2. These 110 old landslides account for 6.7% of the 1649 old landslides and the overlapping area accounts for 2.4% of the total old landslide area (50.3 km^2). The share of the 109 coseismic landslides is 1.9% of the 5,625 landslides and the coverage area (1.2 km^2) is responsible for 2.6% of the total area of the 5,625 landslides. Most overlapping area is characterized by small scars and shallow sliding surfaces; however, some medium landslides (and even large landslides) were also observed. The Horonai giant deep-seated landslide (Fig. 3.5) incorporates one large old landslide and two small old landslides. It should be noted that the overlapping area of the old landslides and the coseismic landslides referred does not mean the reactivation of old landslides in this work.

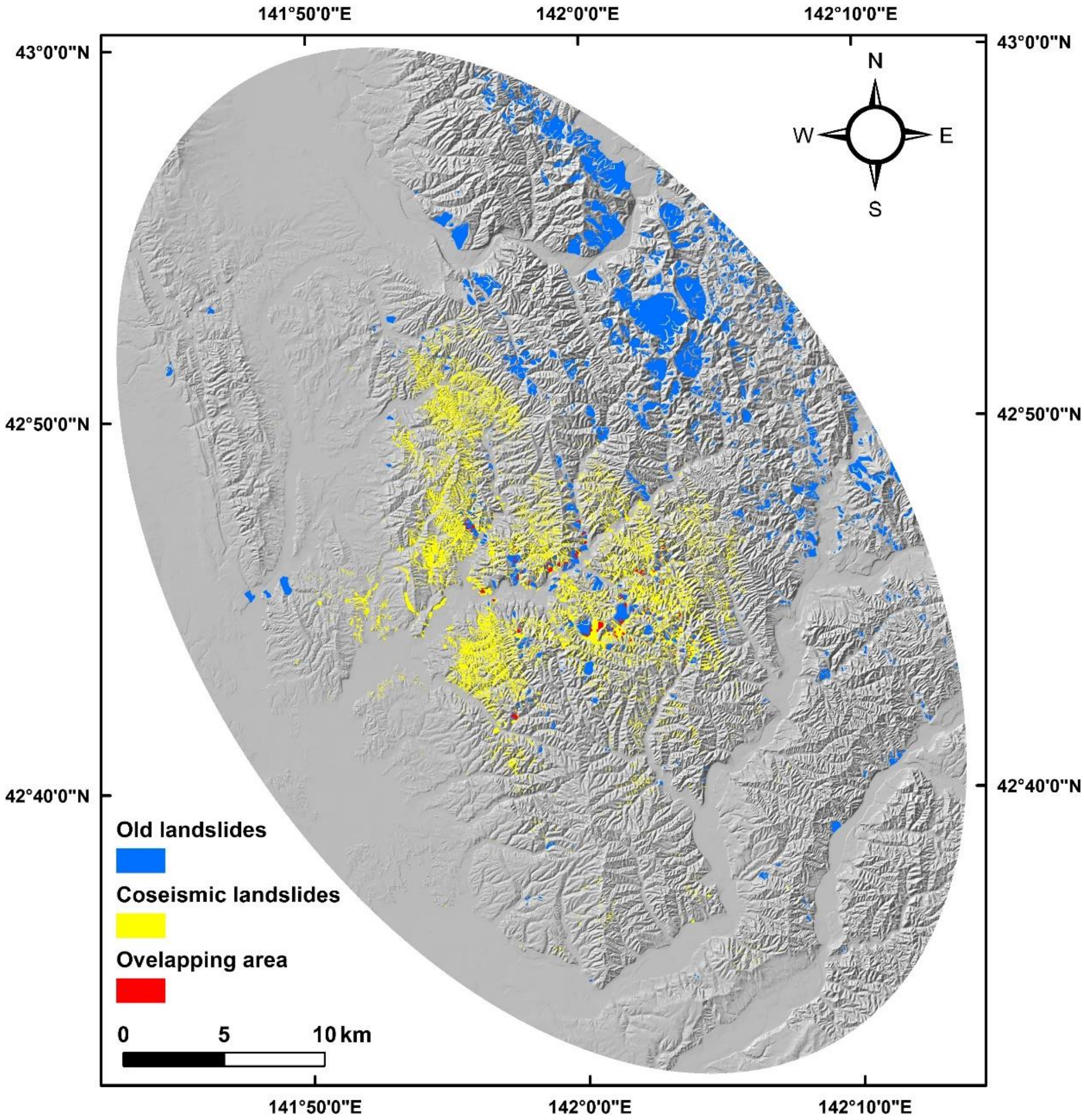

Fig. 3.6 Distribution of the coseismic landslides, the old landslides and the overlapping area of the coseismic landslides and the old landslides

3.5 Possible failure mode

Based on the field reconnaissance and previous literatures (Yamagishi and Yamazaki 2018; Hirose et al. 2018), the Iburi landslides are chiefly shallow translational landslides with planar slip surfaces. Most landslides are characterized by high mobility and long run-out distance, and almost all the upper slip surfaces are exposed without overlapping of sliding mass. It was discovered during the field reconnaissance that the sliding mass moved along the planar interface of the Ta-d pumice and the underlying paleosol. Sliding-zone liquefaction (Sassa et al. 1996; Wang 1999) and grain crushing occurred within the saturated pumice layers (L5, L6 and L7 in Fig. 3.4) during the down-slope motion. The pumice layers were crushed and the thickness was attenuated, which was confirmed by the clear crushed pumice strips during the field work. The crushed and liquified pumice layers spread in the deposition area and resulted in the extension of the upper sliding mass in horizontal directions. In consideration of this, the possible failure mode for the Iburi landslides is depicted in Fig. 3.7. The slope angle after failure remains unchanged as the pyroclastic fall deposits were evenly deposited on the original slope surface (mantle bedding) (Fig. 3.7a). A sharp free face appears at the scarp (Fig. 3.7b) and creates a high possibility of retrogressive slope failure due to future seismic oscillation.

Previous research indicates that the Ta-d layer outcropped in Tomakomai (southwest of the study area) is underlain by earlier pyroclastic fall deposits, such as Spfl, Spfa-1, and Kt-1 (Nakagawa et al. 2018). Thus, it can be inferred that the soil structure below the Ta-d layer in the study area is similar to the typical outcrop in Tomakomai, although the integrity of the lower pyroclastic fall deposits may be different. The strong ground shaking peeled off the well-stratified upper pyroclastic fall deposits and exposed the underlying pyroclastic fall deposits. Moreover, antecedent precipitation and the permeability difference of the ternary “clay-volcanic ash-pumice” structure also exacerbated the occurrence of landslides, as rainwater infiltrated through the coarse pumice vertically and ultimately perched over the fine paleosol which has low permeability.

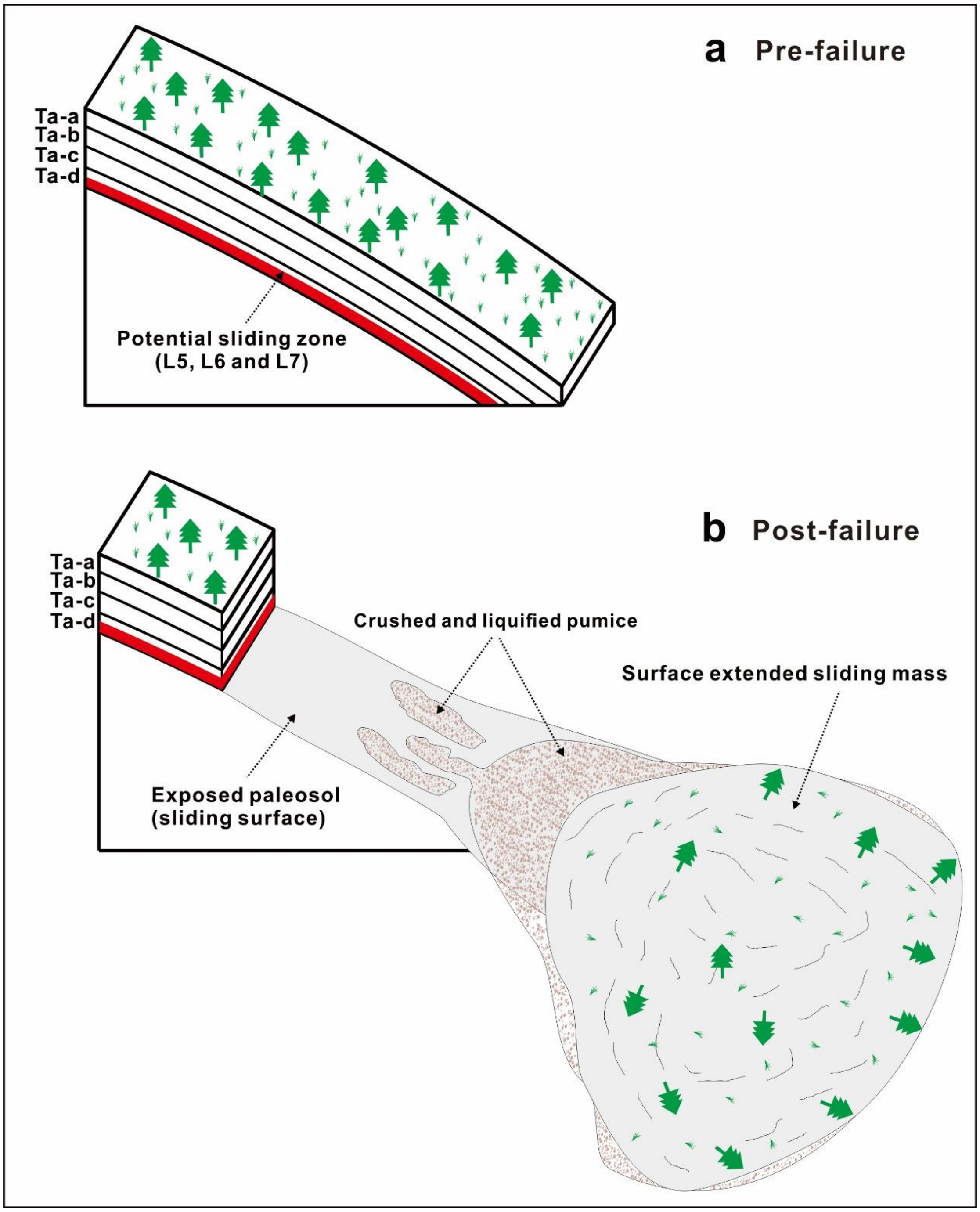

Fig. 3.7 Schematic diagram depicting the failure mode of the coseismic landslides (the pyroclastic fall deposit layers are classified based on Tajika et al. (2016).). **a** Translational landslide before failure. **b** Translational landslide after failure

3.6 Size characterization

The majority of landslides triggered by the Iburi earthquake sequence are small to medium in size. The average area of the Iburi landslides is 8,238 m^2. The dominant range of the slide area is between 100 m^2 and 10,000 m^2, which accounts for 75.6% of the total occurrence (Table 3.1 and Fig. 3.8a). Landslides with an area larger than 100,000 m^2 comprise 0.1% of all landslides, and only 5 landslides (0.1%) were confirmed to be smaller than 100 m^2 (Table 3.1 and Fig. 11a). The relationship between the cumulative number and affected area of the coseismic landslides was expressed as logarithmic coordinates (Fig. 3.8a) and can be approximated by a natural logarithmic function, as expressed in Equation 1.

$$\ln(N_c) = -1.92\ln(A) + 25.14 \tag{3.1}$$

where Nc denotes the cumulative number of landslides with an area greater than or equal to a certain area A. The coefficient of determination of the natural logarithmic function for a landslide area larger than 10,000 m^2 is as high as 0.98. However, the cumulative number of landslides with area smaller than 10,000 m^2 in reality is lower than that suggested by this calculation. Similar logarithmic functions were also described with respect to the landslides triggered by the 2008 Wenchuan earthquake, and the lower Nc below the linear fit curve was attributed to incomplete sampling of small landslides and overlapping of large landslides on small landslides (Dai et al. 2011; Xu et al. 2014). The size of landslides triggered by the Iburi earthquake is about one order of magnitude smaller than that of the landslides investigated in the case of the Wenchuan earthquake. Thus, the lower Nc value observed in this study may be the result of the frequent occurrence of mobilization of valley fill, as this type of landslide incorporates several small landslides.

Table 3.1 Size characterization of landslides triggered by the Iburi earthquake

Area (m^2)	**LSN**	**LSNP (%)**	**Frequency**	**Probability**
0 < A≤100	5	0.1	5.0×10^{-2}	8.9×10^{-6}
100 < A≤1,000	670	11.9	7.4×10^{-1}	1.3×10^{-4}
1,000 < A≤2,000	870	15.5	8.7×10^{-1}	1.6×10^{-4}
2,000 < A≤3,000	602	10.7	6.0×10^{-1}	1.1×10^{-4}
3,000 < A≤4,000	508	9.0	5.1×10^{-1}	9.0×10^{-5}
4,000 < A≤6,000	778	13.8	3.9×10^{-1}	6.9×10^{-5}
6,000 < A≤8,000	497	8.8	2.5×10^{-1}	4.4×10^{-5}
8,000 < A≤10,000	330	5.9	1.7×10^{-1}	2.9×10^{-5}
10,000 < A≤20,000	820	14.6	8.2×10^{-2}	1.5×10^{-5}
20,000 < A≤40,000	415	7.4	2.1×10^{-2}	3.7×10^{-6}
40,000 < A≤60,000	80	1.4	4.0×10^{-3}	7.1×10^{-7}
60,000 < A≤80,000	27	0.5	1.4×10^{-3}	2.4×10^{-7}
80,000 < A≤100,000	15	0.3	7.5×10^{-4}	1.3×10^{-7}
100,000 < A≤600,000	8	0.1	1.6×10^{-5}	2.8×10^{-9}

LSNP (landslide number percentage) is the percentage of landslide number in each class.

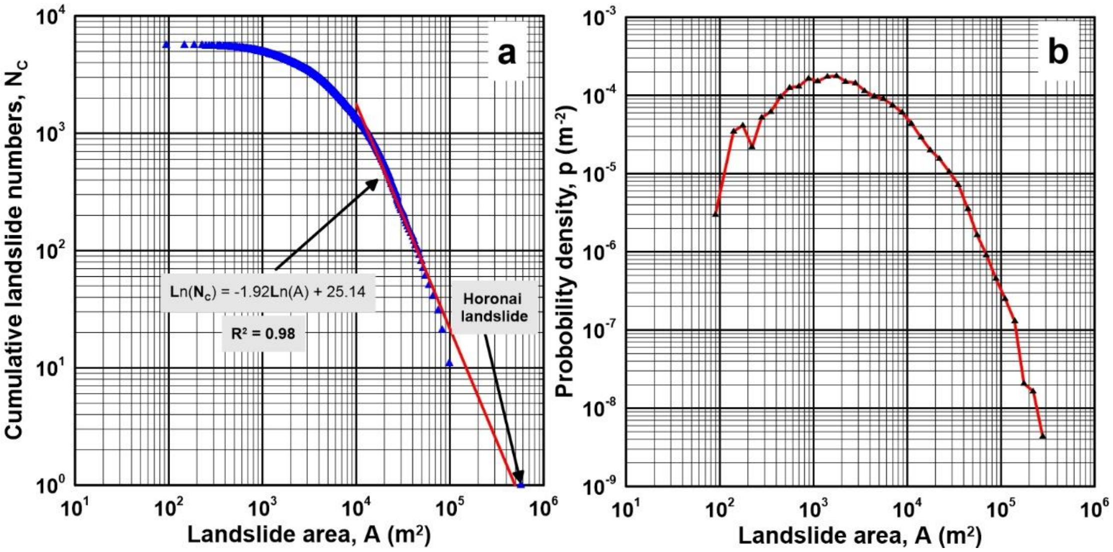

Fig. 3.8 Size distribution of the coseismic landslides in logarithmic forms. **a** Cumulative landslide numbers-size distribution. **b** Noncumulative probability density-size distribution

Frequency density and probability density, which can illustrate the density of landslides in a certain area range, were also analyzed in this work. Frequency density is expressed as the ratio of landslide number (LSN) within a certain area range and the corresponding area interval. Probability density is obtained by dividing the frequency density by total occurrence. In order to study the relationship between the probability density and landslide size, the coseismic landslides (except for the Horonai landslide) are divided into 35 classes (Table 3.2). The classification of the classes is based on the increment of 0.1 for $log\ (A_{max})$, as illustrated in Table 3.2. Figure 3.8b demonstrates the relationship between the probability density and landslide size. The probability density increases with size up to a certain value (between 1,000 m^2 to 1,259 m^2, which represents the most abundant landslide concentration) and decreases thereafter. Even though the probability density-size distribution of the Iburi landslides isn't a pure power-law function as proposed in previous studies (Whitehouse and Griffiths 1983; Hovius et al. 1997; Stark and Hovius 2001; Guzzetti et al. 2002), the general trend matches well with that of the 11,111 landslides induced by the 1994 Northridge earthquake, the 4,233 snowmelt-coseismic landslides of central Italy in 1997, and the 9,594 landslides resulting from the 1998 heavy rainfall in Guatemala (Malamud et al. 2004).

Table 3.2 Classes classified for depicting the probability density-size distribution of the Iburi landslides

Class	**A_{min} (m^2)**	**A_{max} (m^2)**	**Log (A_{max})**	**Area interval**	**Class**	**A_{min} (m^2)**	**A_{max} (m^2)**	**Log (A_{max})**	**Area interval**
1	20.0	79.4	1.9	59.4	**19**	3,981.1	5,011.9	3.7	1,030.8
2	79.4	100.0	2.0	20.6	**20**	5,011.9	6,309.6	3.8	1,297.7
3	100.0	125.9	2.1	25.9	**21**	6,309.6	7,943.3	3.9	1,633.7
4	125.9	158.5	2.2	32.6	**22**	7,943.3	10,000.0	4.0	2,056.7
5	158.5	199.5	2.3	41.0	**23**	10,000.0	12,589.3	4.1	2,589.3
6	199.5	251.2	2.4	51.7	**24**	12,589.3	15,848.9	4.2	3,259.7
7	251.2	316.2	2.5	65.0	**25**	15,848.9	19,952.6	4.3	4,103.7
8	316.2	398.1	2.6	81.9	**26**	19,952.6	25,118.9	4.4	5,166.2
9	398.1	501.2	2.7	103.1	**27**	25,118.9	31,622.8	4.5	6,503.9
10	501.2	631.0	2.8	129.8	**28**	31,622.8	39,810.7	4.6	8,187.9
11	631.0	794.3	2.9	163.4	**29**	39,810.7	50,118.7	4.7	10,308.0
12	794.3	1,000.0	3.0	205.7	**30**	50,118.7	63,095.7	4.8	12,977.0
13	1,000.0	1,258.9	3.1	258.9	**31**	63,095.7	79,432.8	4.9	16,337.1
14	1,258.9	1,584.9	3.2	326.0	**32**	79,432.8	100,000.0	5.0	20,567.2
15	1,584.9	1,995.3	3.3	410.4	**33**	100,000.0	125,892.5	5.1	25,892.5
16	1,995.3	2,511.9	3.4	516.6	**34**	125,892.5	158,489.3	5.2	32,596.8
17	2,511.9	3,162.3	3.5	650.4	**35**	158,489.3	199,526.2	5.3	41,036.9
18	3,162.3	3,981.1	3.6	818.8					

CHAPTER 4

FACTORS AFFECTING LANDSLIDE OCCURRENCE AND DISTRIBUTION

To better understand the general features of the study area and to evaluate the effect of primary and triggering factors on landsliding, three terms in addition to the aforementioned CA (class area), LSN (landslide number) and LSA (landslide area), are introduced in this study. These are T_{LSN} (total landslide number), T_{LSA} (total landslide area), and T_{CA} (total class area). Another two indexes, i.e., LSAP (percentage of landslide area) and CAP (class area percentage), in addition to the above-mentioned LSNP (landslide number percentage) and LC (landslide concentration), are also described herein. LSNP (LSAP) represents the percentage of number (area) of landslides in one class. LC shows the landslide density of certain class. CAP is the area percentage of one class to the total classes. The corresponding equations of these four indexes are expressed in Equation 4.1 to Equation 4.4.

$$LSNP = \frac{LSN}{T_{LSN}} \times 100\% \tag{4.1}$$

$$LSAP = \frac{LSA}{T_{LSA}} \times 100\% \tag{4.2}$$

$$LC = \frac{LSN}{CA} \tag{4.3}$$

$$CAP = \frac{CA}{T_{CA}} \times 100\% \tag{4.4}$$

4.1 Seismological factors

Seismological factors are the overriding variables controlling the occurrence of landslides in the Iburi earthquake sequence. To obtain the relationship between the epicentral distance and landslide distribution, a series of concentric circles centering on the epicenter of the mainshock were selected. Concentric circles with a 1 km incrementing radius were confirmed to be meaningful and reasonable based on a previous study (Keefer 2000). Concentric bands, created by the intersection of the study area and concentric circles, were then employed as the class area (Fig. 4.1a). Figure 4.1b shows concentric bands with an epicentral distance of 5 to 9 km as having the most abundant landslides. The largest LC (9.6 per km^2) appears at an epicentral distance of approximately 7 km. Most landslides are distributed within an epicentral distance of 22 km and the farthest landslide is observed about 32.8 km away from the epicenter (Fig. 4.1b), which is within the maximum epicentral distance limit for both disrupted landslides and coherent landslides as proposed by Keefer (1998). It is surprising that only 4 landslides (LSNP: 0.07%) are distributed in the area within an epicentral distance of 1 km, and only 186 landslides occurred within the surface projection of the seismogenic fault model published by the Geospatial Information Authority of Japan, which is a 14.0 km long and 4.4 km wide rectangle (Figs. 4.2a and 4.2b). The LC of the class with a 1 km epicentral distance is 1.5 per km^2. The LC of the surface projection of the seismogenic fault model is 3.0 per km^2. Both of these are less than that of the study area (ellipse 3 in Fig. 3.1, 3.6 per km^2) and much less than that of the landslide abundant area (ellipse 1 in Fig.

3.1, 21.0 per km^2). In light of this, the controlling effect of the seismogenic fault is not discussed in this work.

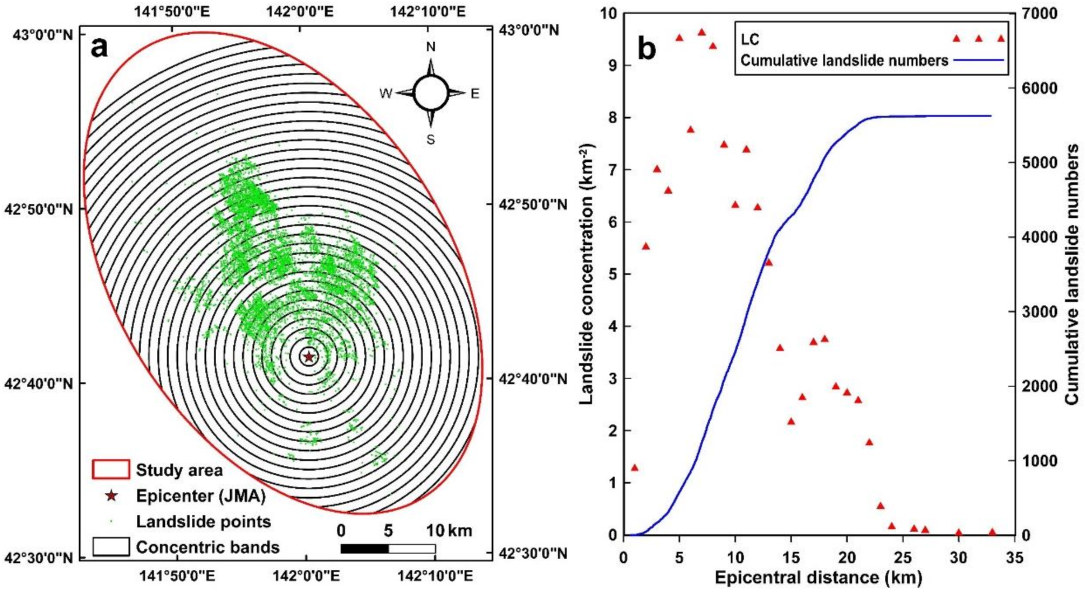

Fig. 4.1 Relationship between landslide occurrence and epicentral distance. **a** Concentric bands with 1-km increment. **b** Landslide concentration and cumulative landslide numbers versus epicentral distance

Peak ground acceleration and seismic intensity are two major indexes reflecting ground motion and shaking during an earthquake. They are also influencing factors controlling the distribution of coseismic landslides. The CAP, LSNP, LSNP, and LC of the seismic intensity classes show high consistency (Fig. 4.2c). Landslides that occurred in classes with seismic intensities between 7.0 and 8.0 account for the majority of the total occurrence, and the high LCs of 5.0 per km^2 and 4.9 per km^2 for these two classes indicate the overriding abundance of landslides. The relatively lower

LC of 1.9 per km^2 of the class with seismic intensity larger than 8.0 can be best explained by the flat topography of this class. The PGA in the study area ranges from 0.1 g to larger than 0.7 g, and only areas with PGA larger than 0.2 g are considered, as all landslides lie in this range. The distribution curve of CAP is in good agreement with that of LSNP. The PGA classes of 0.5 g to 0.6 g and larger than 0.7 g account for the largest and smallest class area with CAPs of 32.9% and 2.2%, respectively. Landslides of these classes also register the largest and smallest portion with LSAPs of 50.0% and 0.4% and LANPs of 39.0% and 0.7%, accordingly (Fig. 4.2d). However, the LC generally decreases with a decrease in PGA. Areas with the most and least abundant landslides, lie in classes with 0.6 g to 0.7 g and 0.2 g to 0.3 g, which effectively demonstrates the controlling effect of PGA on landslide distribution. The relatively lower LC of the class with PGA > 0.7 g may be resulted from the subdued relief of the fluvial terrace in this class.

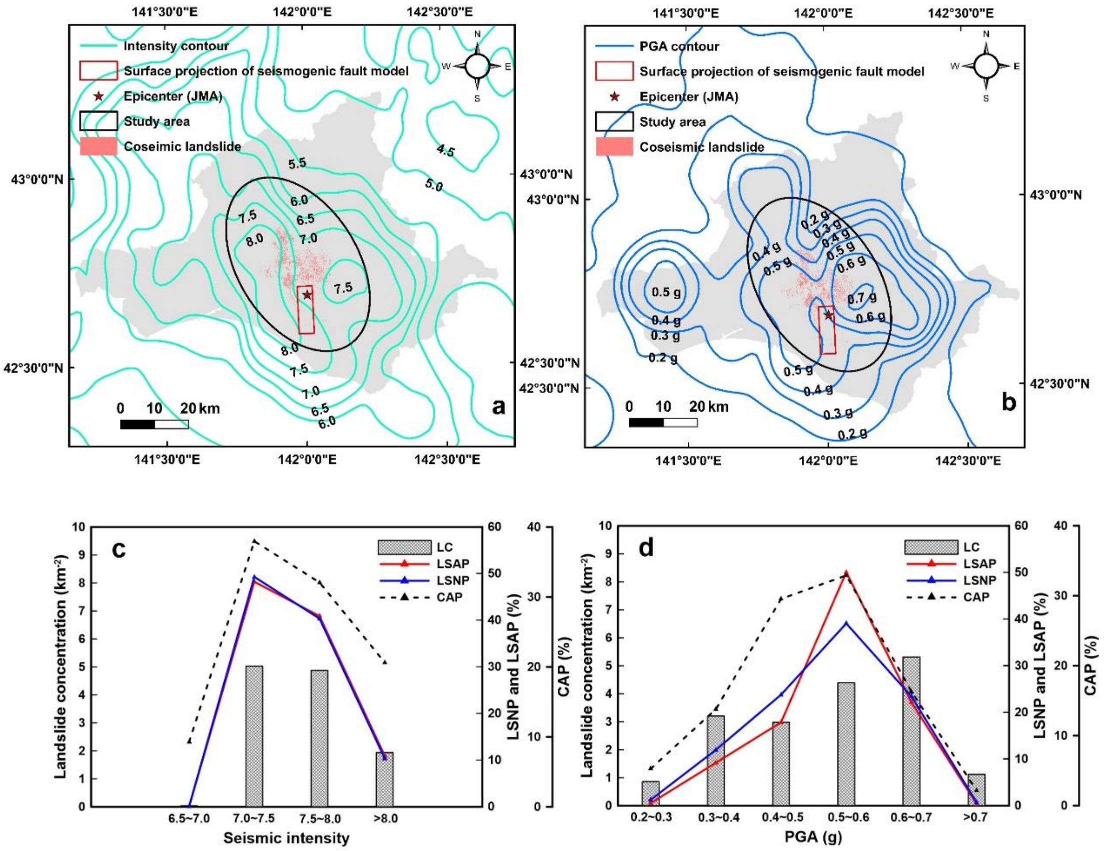

Fig. 4.2 Distribution of Modified Mercalli Intensity contours (**a**) and PGA contours (**b**) published by U.S. Geological Survey and relationships between coseismic landslides and seismic intensity (**c**) as well as PGA (**d**)

4.2 Topography factors

Generally, the rugged alpine terrain is more susceptible to landsliding than subdued topography. Topographic factors such as elevation, slope angle, and slope aspect have been widely used in previous studies to evaluate the influence of such factors on landslide distribution (Xu et al. 2018). The elevation of the study area ranges from 0.2 m to 642.3 m and study area is divided into nine classes. These include eight classes with a 50 m elevation interval and one class with elevations higher than 400 m (Fig. 4.3a). Centroid elevation of the coseismic landslide was employed to represent the elevation of each landslide. Figure 14a indicates that the distribution curve of CAP shows a descending trend with increasing elevation. Two classes with elevations below 100 m register the largest coverage with a CAP of 47.4%. However, the most abundant three classes are characterized by elevations between 100 m and 250 m (100-150 m, 150-200m, and 200-250 m), with the LCs of 7.9 per km^2, 7.6 per km^2 and 4.9 per km^2, respectively. The LANP and LSNP of classes with elevations below 50 m and above 300 m are only 4.4% and 4.5% respectively, despite the CAP of the corresponding classes being as high as 31.3%.

The mean slope angle and mean aspect of all coseismic landslides were calculated using the Zonal Statistics as Table tool in ArcGIS. Figure 4.3d suggests that the study area is predominately covered by classes with a slope angle below 10° and with a CAP of 45.0%. However, landslides are concentrated in classes with a slope angle between 15° and 35°, and the LCs of these four classes are 5.1, 10.0 per km^2, 10.9 per km^2, and 7.5 per km^2, respectively (Fig. 4.3e). The LASP and LSNP of classes with slope angle between 15° and 35° are as high as 87.8% and 85.9%, while the CAP is only 37.0%. Westerly-facing slopes with western, southwestern, and northwestern octants stand out slightly in the study area. The corresponding CAPs are 15.1%, 14.3%, and 13.7%, marginally larger than the average value of 12.5% (Fig. 4.3f). The preferred inclinations of coseismic landslides are south, southwest, and southeast as illustrated by the distribution curve of LC (Fig. 4.3g). The distribution curves of LSAP and LSNP indicate that the preferred orientations of the landslide-affected area are south and southwest, followed by southeast and west (Fig. 4.3f). Therefore, south, southwest, and southeast can be confirmed as the overriding orientation of coseismic landslides triggered by the Iburi earthquake, deviating about 90° anticlockwise from the slightly preferred orientation of the whole study area.

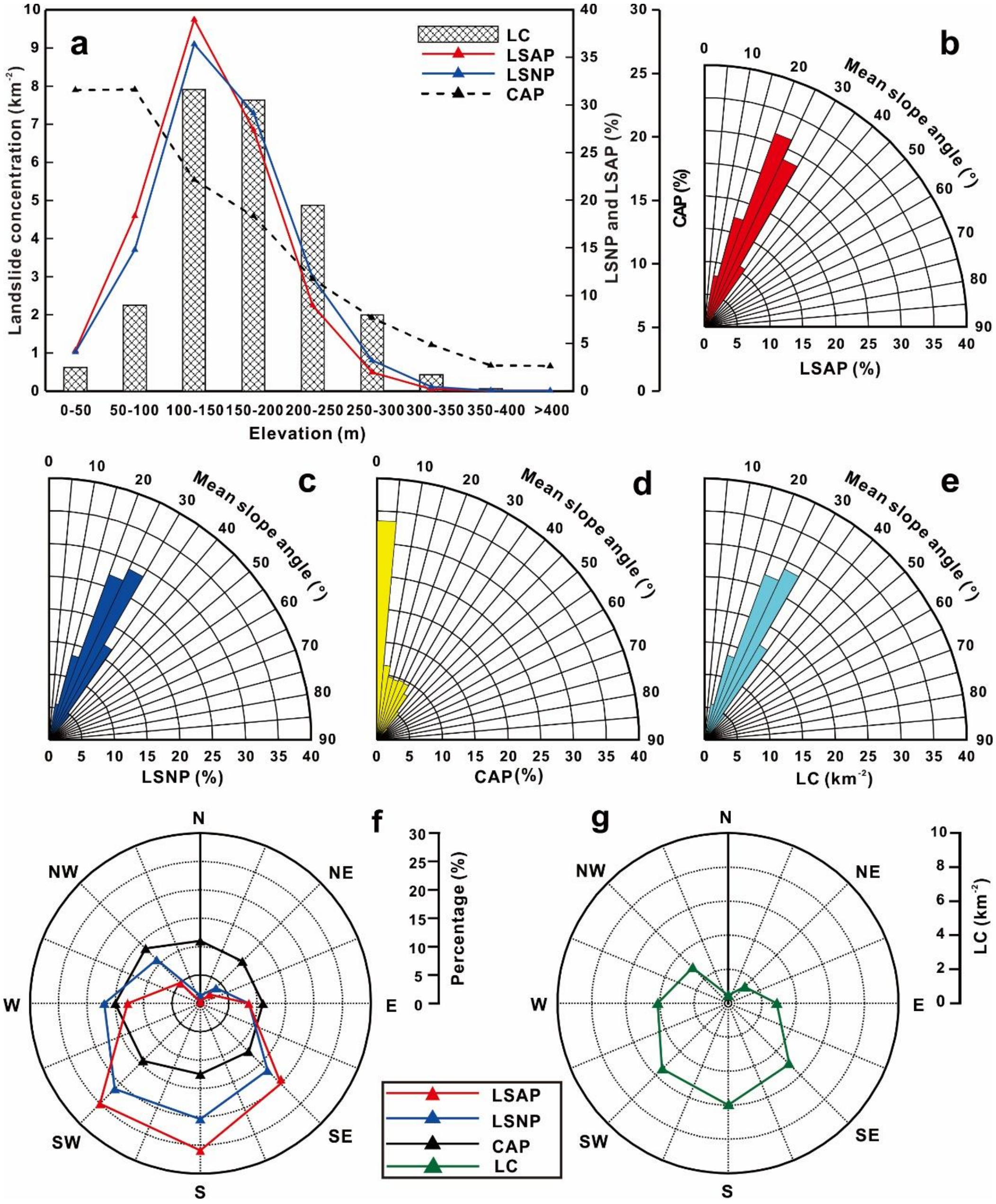

Fig. 4.3 Relationships between coseismic landslides and terrain variables. **a** Landslide concentration, landslide area percentage, landslide number percentage and class area percentage versus elevation. **b** Landslide area percentage versus mean slope angle. **c** Landslide number percentage versus mean slope angle. **d** Landslide concentration versus mean slope angle. **e** Class area percentage versus mean slope angle; **f** Landslide area percentage, landslide number percentage and class area percentage versus mean slope aspect. **g** Landslide concentration versus mean slope aspect

4.3 Geological factors

Even though most of the landslides during the Iburi earthquakes occurred in pyroclastic fall deposits, the lithology of the underlying bedrock may have controlled the distribution of the coseismic landslides, as lithological variation confers different mechanical properties (Xu et al. 2014) and affects the original formation of topography prior to pyroclastic fall deposition. The geology units in the study area were divided into 18 classes incorporating water, and only nine classes were observed to be related to landslide occurrence (Table 2.1 and Fig. 4.4a). Figure 4.4a illustrates landslide occurrence in different geological units. N2sn is the largest class area with the most concentrated landslides with a CAP of 43.0% and a LC of 8.1 per km^2. N3sn with the LC of 2.6 per km^2 is another remarkable class, accounting for 9.2% of the total occurrence and 6.6% of the total affected area. It is worth noting that despite the CAP of Q2sr being only 1.2%, the LC of the class is as high as 1.3 per km^2, which is much higher than that for the other six classes. In order to investigate the correlation of lithology and slope angle, each class (excluding water) was subdivided into eleven subgroups with slope angle at 5° intervals from 0° to 55° and one subgroup having slope angle larger than 55° (Figs. 4.4b and c). Unsurprisingly, the CAP of subgroups with slope angle between 15° and 35° (which is observed as the most likely slope angle for a landslide-affected area) is as high as 57.0% for N2sn. The LC of N3sn is 2.6 per km^2, which is much lower than that of N2sn, even though these two classes are characterized by similar lithology (marine and non-marine sedimentary rocks) and similar seismic intensities between 7.0 and 7.5. This may have resulted from the moderate slope angle of N3sn, as the CAP of subgroups with slope angle between 5° and 20° is 53.2%, which is lower than the most likely slope angle of the landslide area. The low LC of N1sr and PG3sr distributed in the eastern part of the study area may be explained by the significant epicentral distance and weakened shaking during the earthquake sequence. Despite the analogous slope angle (Fig. 4.4c) and lithology (Table 2.1), the LC of Q2sr stands out from Hsr, Q2th, and Q3tl. Of all the 23 landslides occurred in Q2sr, 22 are distributed around the Yoshinoya and Tomisato faults.

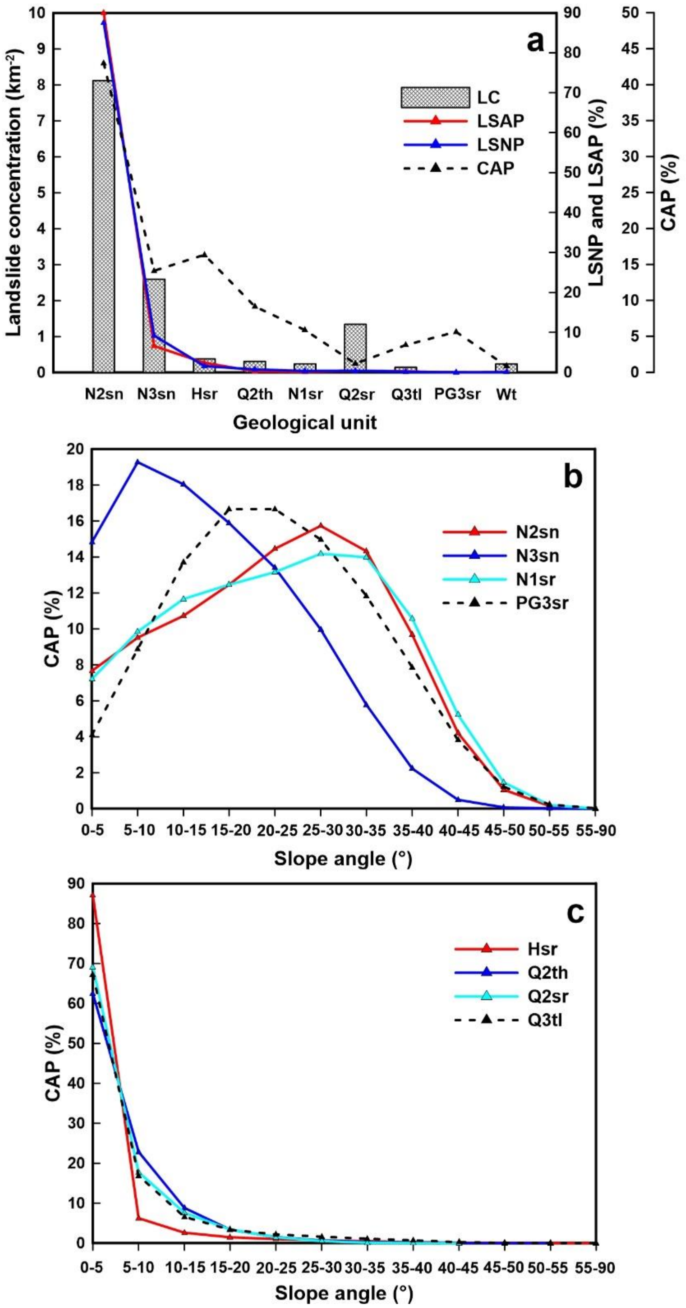

Fig. 4.4 Relationships between coseismic landslides and geological factors. **a** Landslide concentration, landslide area percentage and landslide number percentage in each geological unit and the area percentage of each unit. **b** Subclass area percentage of N2sn, N3sn, N1sr and PG3sr versus slope angle at 5° interval. **c** Subclass area percentage of Hsr, Q2th, Q2sr and Q3tl versus slope angle at 5° interval

In previous cases, distance to seismogenic fault was considered as one of the main factors controlling landslide distribution and the effect of (active) faults was not widely considered in seismic landslides. After further inspection of the general landslide distribution, it is startling to discover that the landslides are distributed approximately symmetrical, centering on the Biratori fault (Fig. 2.5), and the center of three ellipses is only about 220 m away from the Biratori fault. In addition, severe liquefaction and jetted sand in the paddy field (N 42°44'22.26", E 141°54'48.11") were observed in the path of the Yoshinoya fault and Tomisato fault during field investigation. Thus, in order to evaluate the impact of (active) faults on landslide distribution resulting from the Iburi earthquake, the nearest distance from landslide centroid to (active) faults was calculated and then categorized at 100 m intervals. The distribution of LC and LSNP in Fig. 4.5 indicates that both landslide occurrence and landslide concentration generally decrease with increasing distance from fault. The largest LC emerges in the class with a distance between 0.5 km and 0.6 km, while the largest LSNP appears in the class with distance of 0.1 km to 0.2 km. The cumulative LSNP distribution curve reveals that landslide occurrence within a distance of about 1.25 km presents a near linear relationship and also registers the most rapid growth rate. The noticeable negative correlation between landslide occurrence and distance from faults reflects the influence of (active) faults on landslide occurrence.

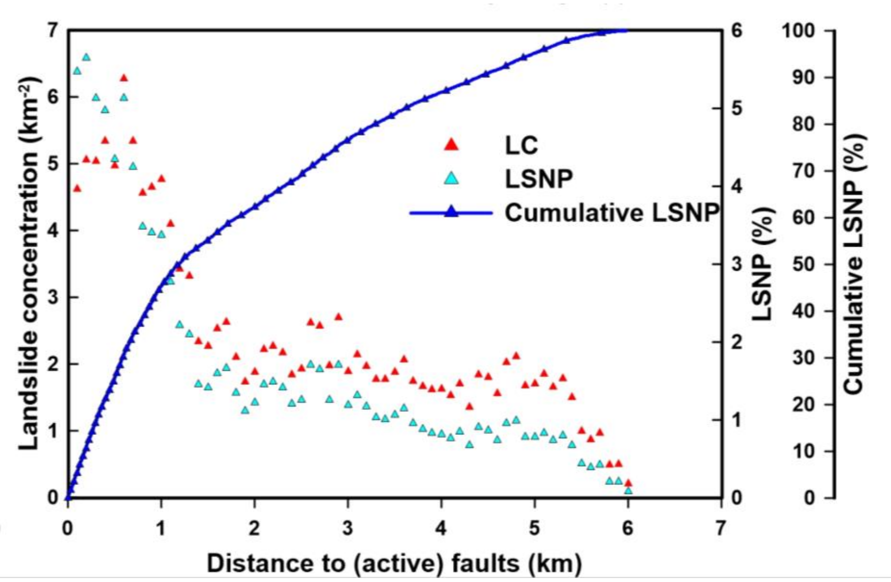

Fig. 4.5 Landslide concentration, landslide number percentage and cumulative landslide number percentage versus distance to (active) faults

CHAPTER 5

THREE-DIMENSIONAL SEISMIC SLOPE STABILITY ASSESSMENT

5.1 Target area and coseismic landslides

The 2018 Hokkaido Eastern Iburi earthquake triggered thousands of landslides in the vicinity of Atsuma, Hokkaido, Japan. In order to evaluate the seismic stability of slopes on a regional scale, four towns in western Atsuma (Fig. 5.1c, Tomisato, Yoshinoya, Sakuraoka and Horosato), where catastrophic landslides occurred, were selected as the calculation area. The calculation area is approximately 12 km from the epicenter of the Iburi earthquake mainshock (Fig. 5.1b). The study area is characterized by moderate terrain with the elevation range of 18 m to 244 m (Fig. 5.2a) and the predominant slope angle below 40° (Fig. 5.2b). As to the slope aspect of the study area, there is no apparent and preferred inclinations (Fig. 5.2c). The majority of study area is underlain by Neogene sedimentary rock (sandstone, siltstone, mudstone and conglomerate) and details of the bedrock classification in the study area are shown in Figure 2d and Table 5.1.

Table 5.1 Classification of geological units in the study area

Code	**Age**	**Lithology**
N2sn	Middle to Late Miocene	Sandstone, mudstone, conglomerate and sandstone (with tuff)
N3sn	Late Miocene to Pliocene	Diatomaceous siltstone with sandstone and conglomerate
Hsr	Late Pleistocene to Holocene	Clay, silt, sand, gravel and peat
Q2th	Middle Pleistocene	Mud, sand, gravel and peat
N1sr	Early Miocene to Middle Miocene	Mudstone, sandstone and conglomerate (with tuff)
Q2sr	Middle Pleistocene	Mud, sand, gravel and peat
Q3tl	Late Pleistocene	Mud, sand, gravel, peat and volcanic materials

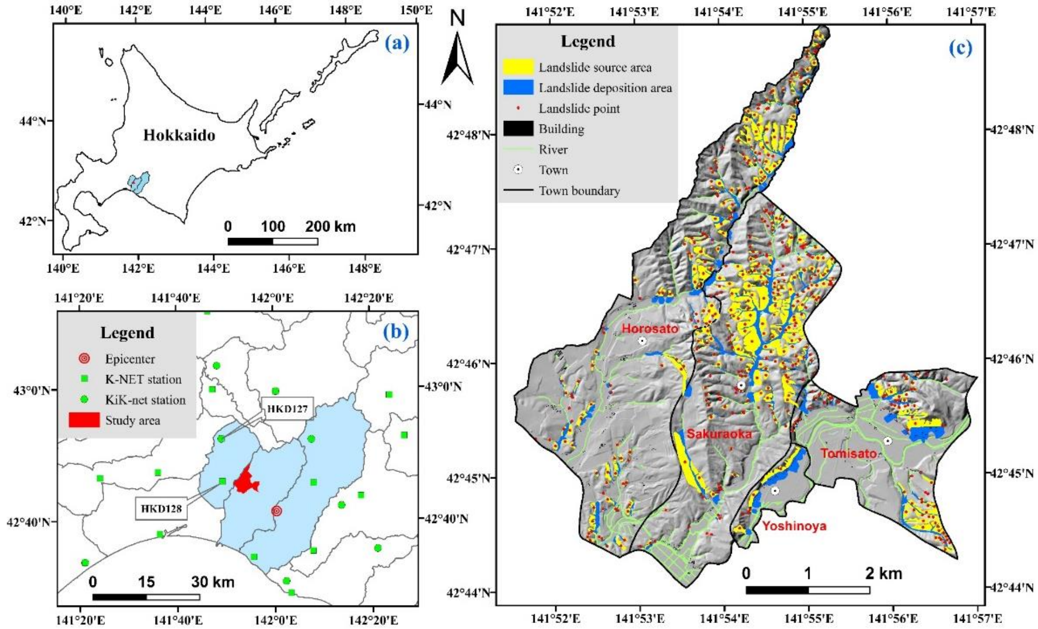

Fig. 5.1 Location maps and coseismic landslides in the study area **(a)** General view of the study area. **(b)** Realtime ground-motion monitoring stations (K-NET station and KiK-net station) distributed around the study area. **(c)** Coseismic landslides triggered by the Iburi earthquake in the study area. The shaded relief map was generated from a 5×5m DEM

During the Iburi earthquake sequence, the highest ground motion was recorded by a K-NET (Kyoshin network) station (HKD127, Fig. 1b) in Abira and the peak ground acceleration (PGA) of this station was approximately 1.83 g (1,796 gal). The intense ground shaking resulted in severe liquefaction and catastrophic damages to houses, roads and other engineering structures. As is revealed in Figure 5.3, severely destroyed road, jetted sand, uplift of inlet well and surface ruptures were observed in the paddy field in Yoshinoya. Moreover, thousands of slope failures were triggered due to the strong Iburi earthquake and 36 persons were killed by the destructive slope failures (Yamagishi and Yamazaki 2018). The damage caused by the slope failures is more extensive than that resulted directly from the earthquake. The study area includes 345 landslides triggered by the Iburi earthquake, and all of these landslides were shallow landslides with long run-out distance and high mobility. Figure 5.4 shows two most destructive landslides, i.e., the

Yoshinoya landslide and the Tomisato landslide in the study area. These two landslides destroyed and buried dozens of houses and other engineering structures at the lower footslope.

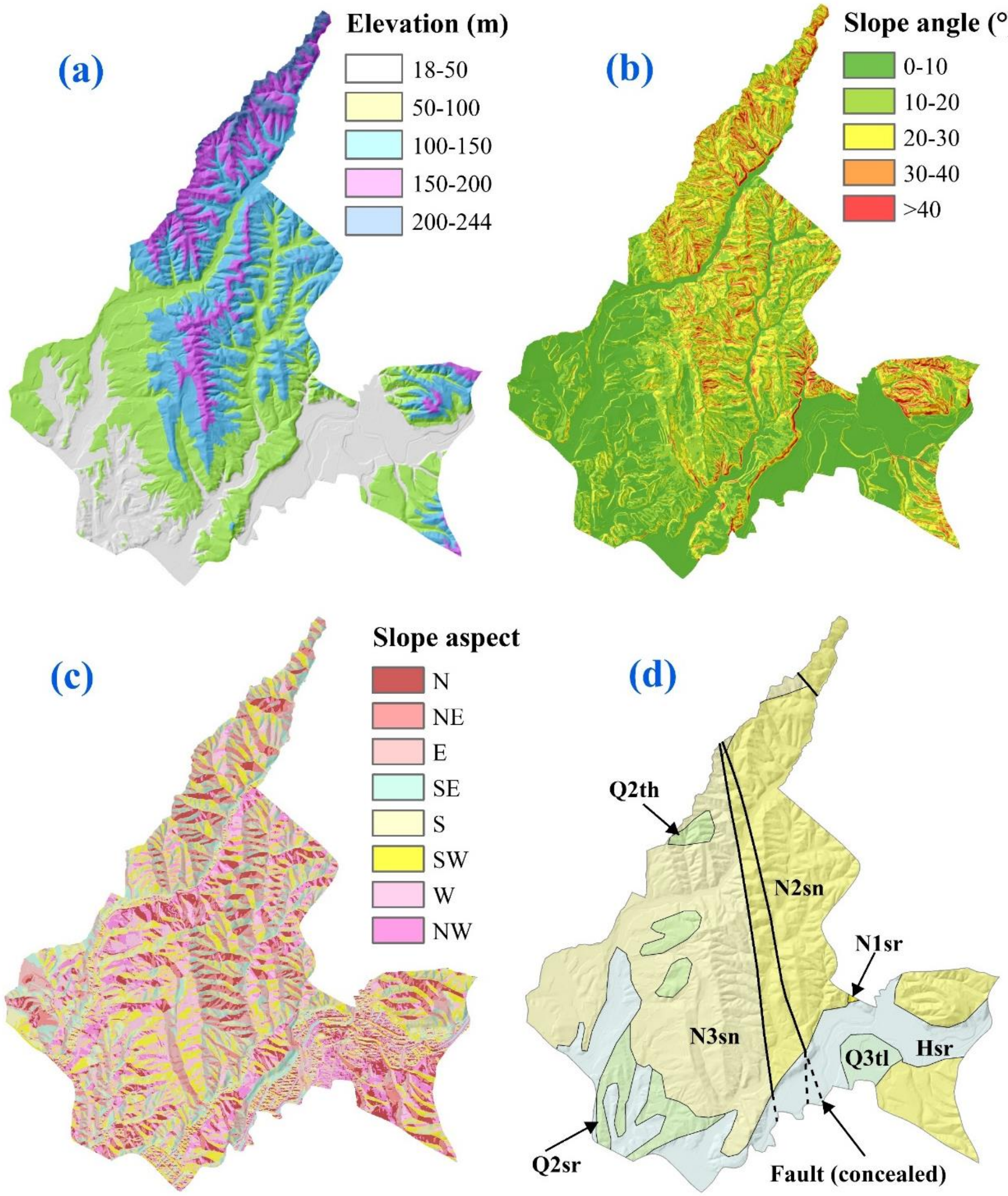

Fig. 5.2 Topographic and geological information of the study area **(a)** Elevation. **(b)** Slope angle. **(c)** Slope aspect. **(d)** Geological map (based on the 1:200,000 seamless geological map published by the Geological Survey of Japan, AIST). The detailed explanations of the geological codes (N2sn, N3sn, Hsr, Q2th, N1sr, Q2sr and Q3tl) are listed in Table 1

Fig. 5.3 Damages and liquefactions resulted from the Iburi earthquake sequence. **(a)** Liquefaction and jetted sand in the paddy field. **(b)** Road damage. **(c)** Uplift of inlet well. **(d)** Surface rupture in the paddy field

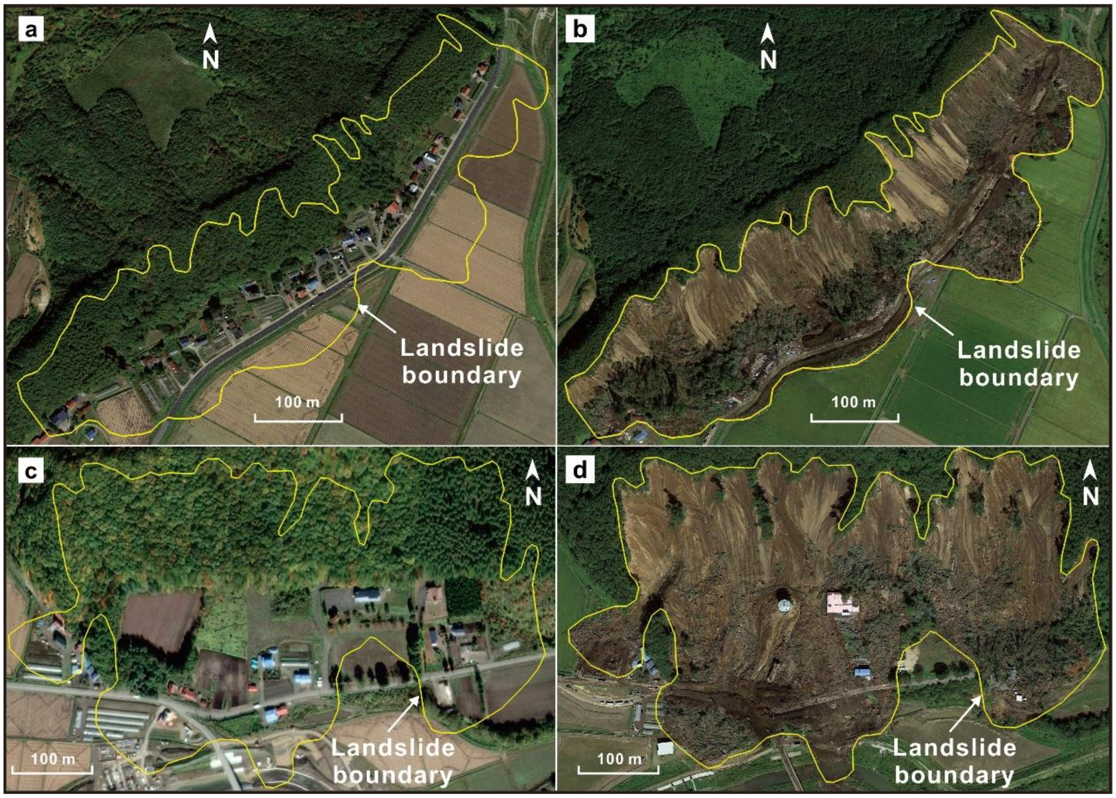

Fig. 5.4 Panoramic views of the destructive Yoshinoya landslide and Tomisato landslide (the base maps are from Google Earth). **(a)** Yoshinoya landslide before failure. **(b)** Yoshinoya landslide after failure. **(c)** Tomisato landslide before failure. **(d)** Tomisato landslide after failure

5.2 Material and methods

The Fortran program Scoops3D, developed by the U.S. Geological Survey has advantages in seismic slope stability calculation on a regional scale, as it can compute the factor of safety of millions of potential landslides based on a predisposed DEM utilizing 3D method of columns approach (Reid et al. 2015). In this work, the user-defined DEM was served as the ground surface and the isopachs of pyroclastic fall deposits around the study area were used to define the depths of soil layers. Then a series of horizontal pseudo-acceleration coefficient proposed in previous studies were applied in seismic slope stability calculation of the study area.

5.2.1 Soil structure and geotechnical parameters

The study area is mantled with late Pleistocene and Holocene pyroclastic fall deposits (Hirose et al. 2018) originated from the Tarumae crater, the Eniwa crater and the Shikotsu crater. According to the eruption ages of the craters, the surface pumice layers around the study area can be classified as six layers, i.e., Tarumae-a (Ta-a, AD1739), Tarumae-b (Ta-b, AD1667), Tarumae-c (Ta-c, 2.5-3 ka), Tarumae-d (Ta-d, 8-9 ka), Eniwa-a (En-a, 20 ka) and Shikotsu-1 (Spfa-1, 40 ka) (Hirose et al. 2018; Tajika et al. 2016). The thicknesses of these six pyroclastic fall deposits in the vicinity of the study area were illustrated in Figure 5.5. The thicknesses of Ta-a, Ta-b, Ta-c, Ta-d, En-a and Spfa-1 pyroclastic fall deposits are 0~0.16 m, 0~0.32 m,0.32 m, 0.3~0.5 m,0.5~1.0 m and 4 m respectively. Considering that the formation age of Ta-a is close to that of Ta-b and the thicknesses of these two layers are very thin compared with other pyroclastic fall deposits, the Ta-a and Ta-b layers are regarded as one layer, Ta-a, b, in this work. During the computation of slope stability analysis, boundary condition is a major concern. To reduce the effect irregular shape of the targeted area on the computation, the rectangle encompassing the study area is chosen as the computation area. Based on the isopachs of pyroclastic fall deposits, the rectangular computation area can be divided into 6 sub-areas. The soil structures of the corresponding sub-areas are depicted in Figure. 5.6.

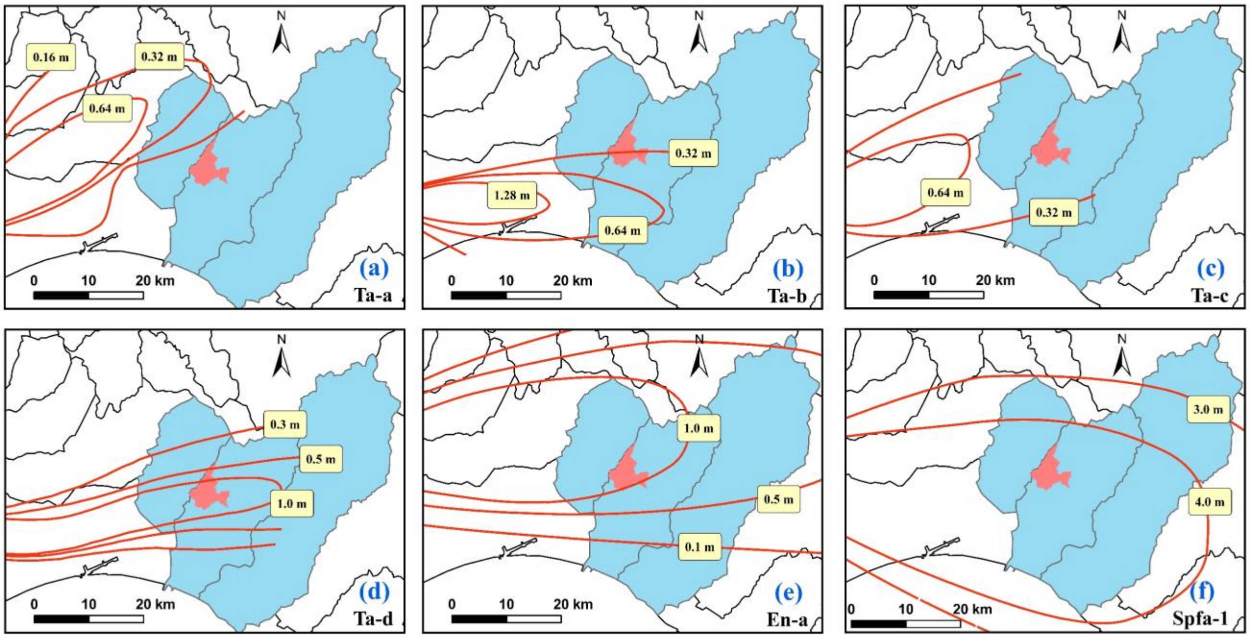

Fig. 5.5 Isopachs of pyroclastic fall deposits (Ta-a, Ta-b, Ta-c, Ta-d, En-a and Spfa-1) in the vicinity of the study area based on Machida and Arai (2003), Furukawa and Nakagawa (2010) and Hirose et al. (2018)

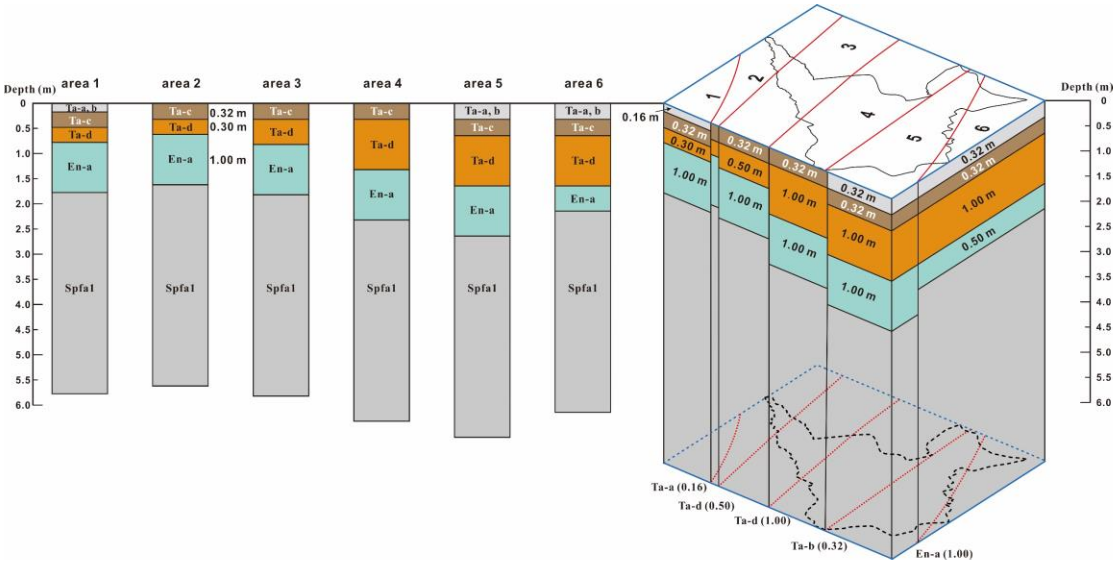

Fig. 5.6 Soil layers and corresponding depths of the six sub-areas classified based on the isopachs of pyroclastic fall deposits

On the basis of our on-site field reconnaissance from 10 September 2018 and the preliminary report (Hirose et al. 2018), the sliding zone of the majority of the Iburi landslide is located in the Ta-d layer. Geotechnical parameters of the pyroclastic fall deposits in the study area are listed in Table 5.2. The basic parameters (bulk weight, saturated unit weight, water content, degree of saturation and void ratio) of Ta-a, b, Ta-c, En-a and Spfa-1 layers are based on previous literature (Miura et al. 2003; Miura and Yagi 2005) and the basic parameters of Ta-d layer are based on samples taken from Tomisato during the field work. The effective strength parameters (effective cohesion and effective friction angle) of En-a and Spfa-1 layers are from the consolidated undrained triaxial test (Miura and Yagi 2005) and the strength parameters (cohesion and friction angle) of Ta-a, b, Ta-c and Ta-d layers utilized in the work are the empirical value from the report of Chuo Kaihatsu Corporation.

Table 5.2 Geotechnical parameters of the pyroclastic fall deposits in the study area

Soil layer	**Soil symbol**	γ_t **(kN/m^3)**	γ_{sat} **(kN/m^3)**	***w*** **(%)**	***Sr*** **(%)**	***e***	***c/c′*** **(kPa)**	***φ/φ′*** **(°)**	**Sampling depth (m)**
1	Ta-a, b	**13.2**	17.2	20	36	1.5	**40**	**20**	unknown
2	Ta-c	**14.7**	17.2	25	46	1.5	**40**	**20**	unknown
3	Ta-d	**12.3**	13.0	138	91	4.0	**40**	**20**	1.7
4	En-a	12.4	**14.7**	65	67	2.8	**74**	**27**	2.2-3.0
5	Spfa-1	9.7	**12.9**	77	57	3.1	**95**	**32**	6.5

γ_t: total unit weight, γ_{sat}: saturated unit weight, *w*: water content, *Sr*: degree of saturation, *e*: void ratio, *c/c′*: (effective) cohesion, *φ/φ′*: (effective) friction angle.

5.2.2 Seismic loading

Earthquake is the predominate factor controlling the occurrence of the Iburi landslides. In order to incorporate the effect of seismic loading in the slope stability computation, the ground acceleration of a distal K-NET station (HKD128) was described in the work. K-NET is a nation-wide strong-motion monitoring network operated by the National Research Institute for Earth Science and Disaster Prevention (NIED) and can send strong-motion data on the Internet. More than 1,000 K-NET stations are distributed uniformly in Japan with a distance of 20 km and the seismograph installed on the ground surface will record the ground accelerations of three directions (east-west (EW), north-south (NS) and up-down (UD)) at each station (Kinoshita 1998). Figure 5.7 shows the monitored ground accelerations of three orthogonal directions (EW, NS and UD) observed by a distal K-NET station (HKD128) during the mainshock of the Iburi earthquake. The HKD128 station is about 6 km west to the study area (Fig. 5.1). The maximum ground accelerations in EW, NS and UD directions are 0.681 g, 0.567 g and 0.404 g respectively (Fig. 5.7). The corresponding time of the maximum ground accelerations in three directions emerges at 26.3 second, 26.5 second and 24.3 second respectively, which indicates the propagation velocity difference of the S wave and P wave.

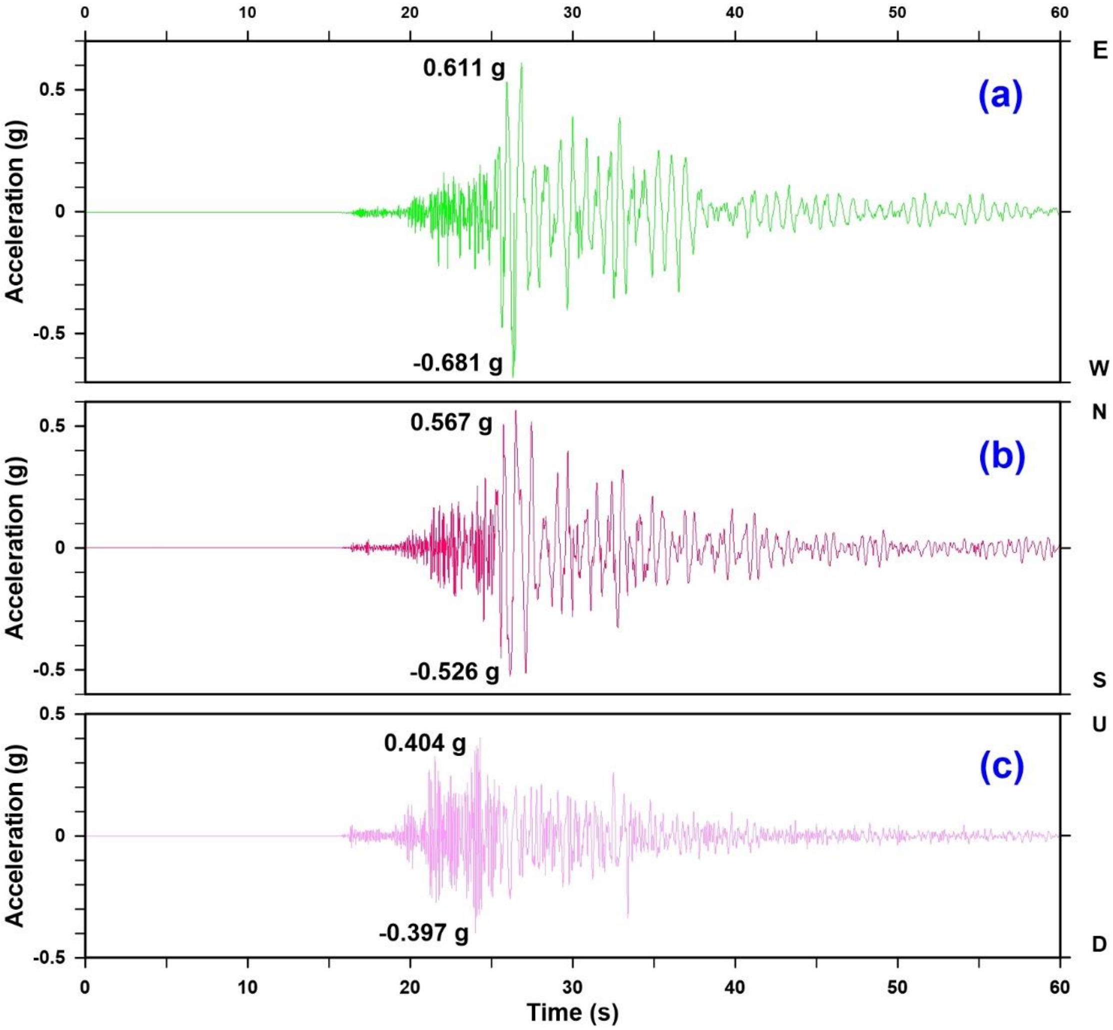

Fig. 5.7 Ground accelerations of three orthogonal directions (EW, NS and UD) observed by a K-NET station (HKD128) in Iburi earthquake. **(a)** Ground acceleration in EW direction. **(b)** Ground acceleration in NS direction. **(c)** Ground acceleration in UD (up and down) direction. The ground acceleration data are derived from the National Research Institute for Earth Science and Disaster Prevention (NIED)

In seismic assessment of slope stability, it is difficult to consider the seismic effect in three directions and the synthetic ground acceleration in horizontal direction is usually employed to simulate the effect of seismic loading. Figure 5.8 displays the synthetic ground accelerations of two dimensions (EW and NS) and three dimensions (EW, NS and UD). The peak horizontal ground acceleration (PHGA) and the peak horizontal ground acceleration are observed at 26.3

second and 26.5 second respectively. The corresponding values of PHGA and PGA are 0.715 g and 0.730 g. As the horizontal seismic loading plays more important role in triggering slope failures and value of PHGA is close to the value of PGA, only horizontal seismic loading was considered in the calculation and the value of PHGA was applied in this work.

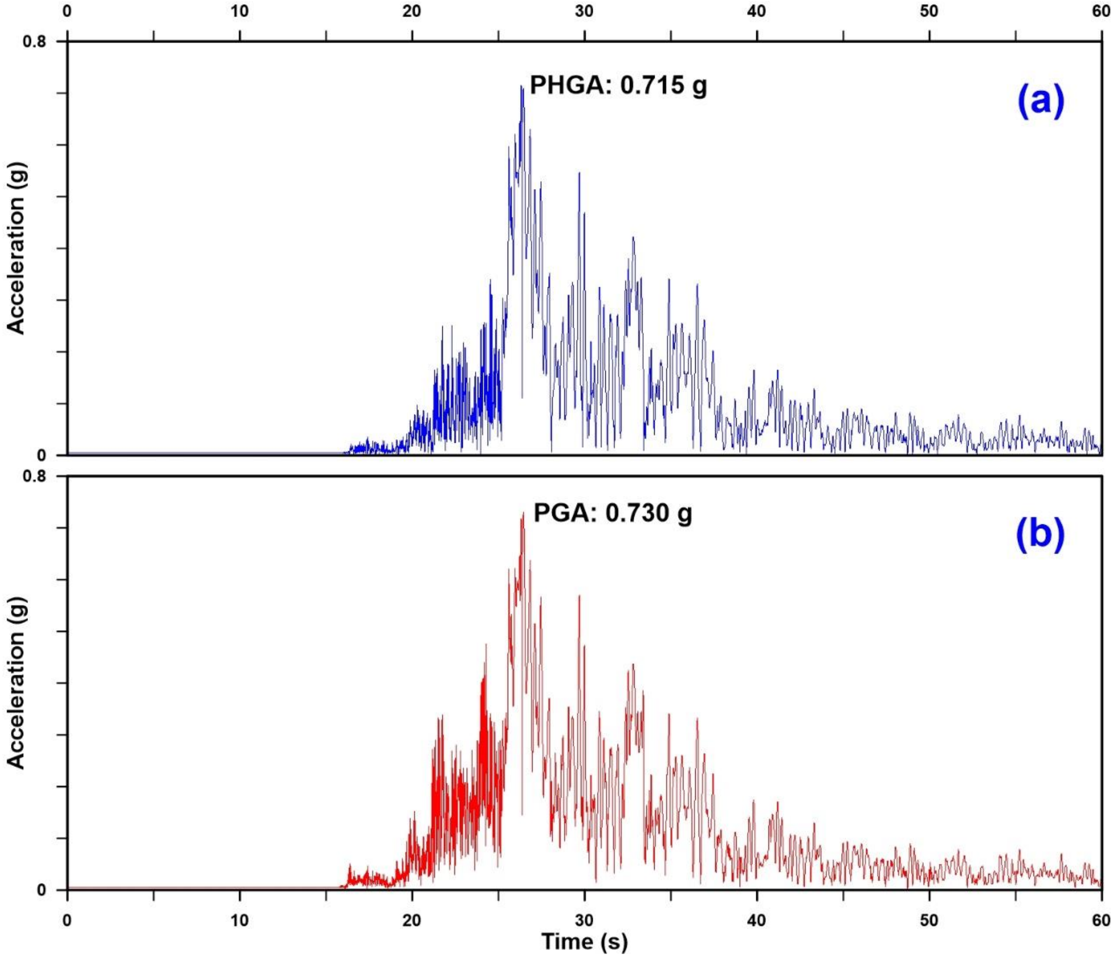

Fig. 5.8 Synthetic ground accelerations of two dimensions (EW and NS) and three dimensions (EW, NS and UD) observed by a K-NET station (HKD128) during the Iburi earthquake. **(a)** Horizontal ground acceleration (synthesis of EW and NS directions). **(b)** Total ground acceleration (synthesis of EW, NS and UD directions). The ground acceleration data are derived from the National Research Institute for Earth Science and Disaster Prevention (NIED)

5.2.3 Three-dimensional slope stability analysis

Scoops3D computes the stability of rigid masses encompassed by the spherical trial surfaces (potential sliding surfaces) and the topography, and assesses slope stability by extending conventional limit-equilibrium analysis to three dimensions. It uses a 3D method-of-columns approach to compute the factor of safety in a 3D domain (Reid et al. 2015). By defining a series of rotational center and gradually increased radii, numerous potential sliding surfaces intersected by the spheres and DEM are generated. Then the factor of safety of each potential sliding mass (grid-based) is calculated by either Bishop's simplified method or the ordinary method (Reid et al. 2015). As Bishop's simplified method provides more accurate solutions of factor of safety (F_S) and the value of F_S is similar to some rigorous limit equilibrium methods (Spencer 1967; Hungr 1987; Lam and Fredlund 1993; Reid et al. 2015; Tran et al. 2018), the slope stability calculation of this work is conducted utilizing Bishop's simplified method.

In moment equilibrium methods, the factor of safety can be expressed as the ratio of shear strength (τ) to the shear stress (s) (Reid et al. 2015). Thus, the factor of safety is expressed in Equation 5.1. Figure 5.9 shows the 3D view of one column intersected by the potential sliding surface and DEM as well as the forces acting on this column. The shear strength (τ) is calculated based on the Coulomb-Mohr failure criterion in Equation 5.2.

$$F_s = \frac{\tau}{s} \tag{5.1}$$

$$\tau = c' + (\sigma_n - u)\tan\phi' \tag{5.2}$$

where c' is the cohesion, ϕ' is the internal friction angle, σ_n is the normal stress, and u is the pore water pressure. Based on the global moment equilibrium, the total resisting moment is equal to the driving moment. Considering all the columns encompassed by the spherical trial surface, the factor of safety can be expressed in Equation 5.3.

$$F = \frac{\sum R_{i,j}(c_{i,j}A_{i,j}+(N_{i,j}-u_{i,j}A_{i,j})tan\phi_{i,j})}{\sum W_{i,j}(R_{i,j}sin\alpha_{i,j}+k_{eq}e_{i,j})} \tag{5.3}$$

where $N_{i,j}$ is the normal force of column i,j, $W_{i,j}$ is the weight, $A_{i,j}$ is the area of the trial surface, $R_{i,j}$ is the distance from the rotation axis to the geometric center of the potential sliding face of column i,j, $e_{i,j}$ is the horizontal driving force moment arm, $\alpha_{i,j}$ is the apparent dip angle and k_{eq} is the horizontal pseudo-acceleration coefficient. The factor of safety expressed in Equation 5.3 is suitable for all general moment equilibrium method, and the normal force can be further obtained by the force equilibrium in vertical and horizontal directions in Bishop's simplified method. Then by substituting the calculated normal force from the force equilibrium into Equation 5.3, the factor of safety is finalized as Equation 5.4.

$$F_s = \frac{\sum \frac{R_{i,j}\left[c_{i,j}A_{h_{i,j}}+\left(W_{i,j}-u_{i,j}A_{h_{i,j}}\right)tan\phi_{i,j}\right]}{m_{\alpha_{i,j}}}}{\sum W_{i,j}(R_{i,j}sin\alpha_{i,j}+k_{eq}e_{i,j})} \tag{5.4}$$

where $A_{h_{i,j}}$ is the projected area of the trial surface in horizontal plane ($A_{h_{i,j}} = A_{i,j}\, cos\, \varepsilon_{i,j}$) and $m_{\alpha_{i,j}} = \cos \varepsilon_{i,j} + (sin\alpha_{i,j} tan\phi_{i,j})/F_s$. As is described in Figure 9, $\varepsilon_{i,j}$ is the true dip angle of the trial surface. More details of the theory and operation of Scoops3D can be accessible in the manual book (Reid et al. 2015) published by the U.S. Geological Survey (https://www.usgs.gov/software/scoops3d).

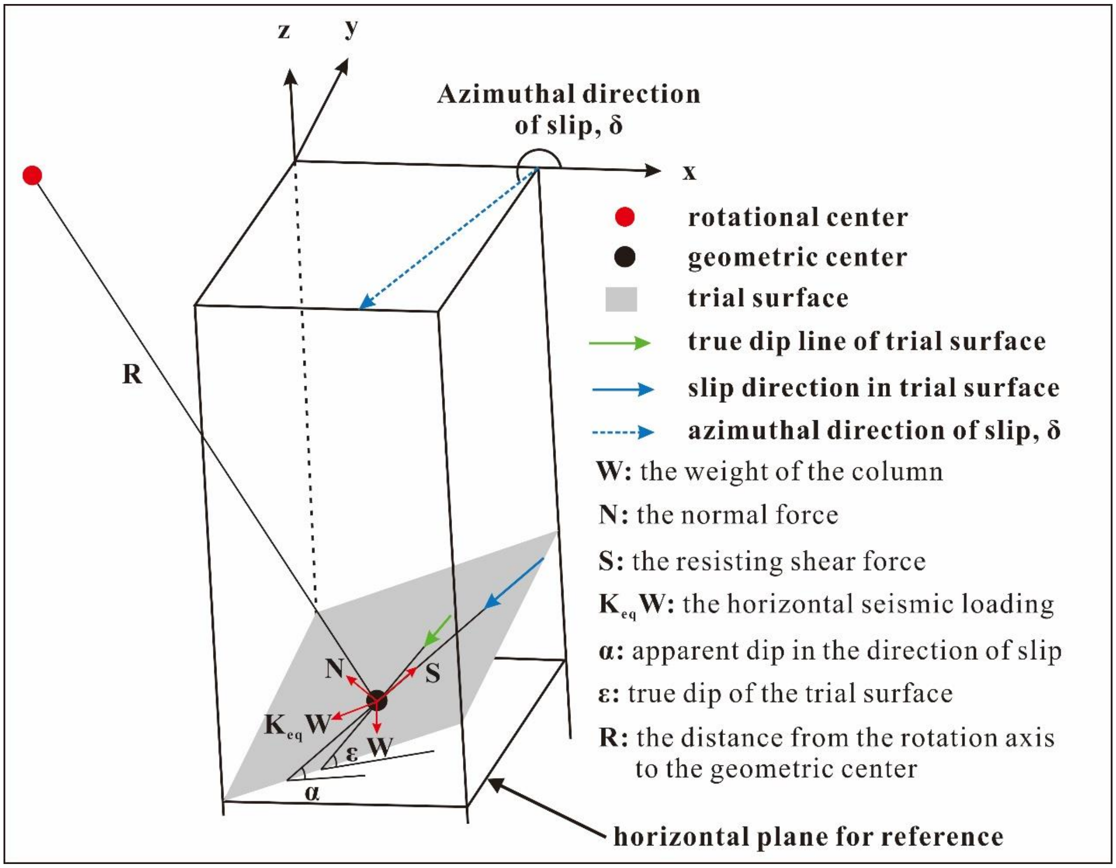

Fig. 5.9 Schematic diagram of forces acting on one column of (modified from Reid et al. (2015))

5.2.4 Input parameters and assumptions

In general, the operation of slope stability calculation in Scoops3D consists of three parts, i.e., construction of 3D domain, input of subsurface parameters and seismic loading, and definition of search configuration. In this work, the 3D domain is layer-based, and the ascii DEM (5×5m) is inputted as the ground surface. The base elevations (bottom) of the pyroclastic fall deposits below the ground surface were calculated using the raster calculator tool in ArcGIS based on the isopachs of pyroclastic fall deposits. In order to ensure the accuracy of base elevations of the soil layers, 30 points (5 points in each sub-area) distributed randomly in the calculation area were selected. Then the elevation of each layer in each point was extracted and the corresponding depths of the soil layers of the 30 points were calculated (Table 5.3). The depths of soil layers of the 30 points show high consistency with depths of soil layers depicted in Figure 5.6. Another consideration during the construction of 3D domain is the location of groundwater table. Based on the samples from

Ta-d layer in Tomisato, the Ta-d layer is highly saturated but not fully saturated (Table 5.2). Due to the scarcity of the information about the variation of groundwater in the study area, which is being loosely populated, the ground water configuration in this work is assumed to be a piezometric surface located at the bottom of the Ta-d layer.

The input geotechnical parameters of soil layers are listed in Table 5.2. A major concern in this part is the selection of a proper horizontal pseudo-acceleration coefficient for the regional stability assessment. Several plausible horizontal seismic coefficients were proposed in previous literatures. Terzaghi (1950) proposed horizontal seismic coefficient of 0.5 is suitable seismic stability assessment for catastrophic earthquakes and Marcuson and Franklin (1983) noted that a value between 1/2 of PHGA and 1/3 of PHGA could be applied as the horizontal seismic coefficient. Other widely applied horizontal seismic coefficients are described in Table 5.4 and eight cases with different horizontal seismic coefficients were selected to simulate the seismic loading in the calculation.

The search configuration includes size criteria of potential slope failures and definition of search extent. 345 coseismic landslides are distributed in the study area and these landslides can be classified as two types, i.e., coherent shallow debris slide and disrupted mobilization of valley fill. 473 landslide source areas were confirmed after a further division of source area and deposition area. More than 90% of the landslide source areas are between 50 m^2 to 20,000 m^2, thus this range is set as the size criteria for potential failures. The horizontal search extent of rotational centers is same with the extent of the study area. The vertical extent of rotational centers ranges from 20 m to 500 m.

Table 5.3 Elevations and depths of the pyroclastic fall deposits in the six sub-areas

Sub-area	Elevation of ground surface	Elevation of Ta-a, b (m)	Elevation of Ta-c (m)	Elevation of Ta-d (m)	Elevation of En-a (m)	Depth of	Depth of Ta-c (m)	Depth of Ta-d (m)	Depth of En-a (m)
1	128.04	127.88	127.56	127.26	126.26	0.16	0.48	0.78	1.78
	76.72	76.56	76.24	75.94	74.94	0.16	0.48	0.78	1.78
	60.44	60.28	59.96	59.66	58.66	0.16	0.48	0.78	1.78
	62.48	62.32	62.00	61.70	60.70	0.16	0.48	0.78	1.78
	102.95	102.79	102.47	102.17	101.17	0.16	0.48	0.78	1.78
2	164.60	164.60	164.28	163.98	162.98	0.00	0.32	0.62	1.62
	201.82	201.82	201.50	201.20	200.20	0.00	0.32	0.62	1.62
	209.04	209.04	208.73	208.43	207.43	0.00	0.32	0.62	1.62
	196.14	196.14	195.82	195.52	194.52	0.00	0.32	0.62	1.62
	191.47	191.47	191.15	190.85	189.85	0.00	0.32	0.62	1.62
3	170.83	170.83	170.51	170.01	169.01	0.00	0.32	0.82	1.82
	159.98	159.98	159.66	159.16	158.16	0.00	0.32	0.82	1.82
	122.11	122.11	121.79	121.29	120.29	0.00	0.32	0.82	1.82
	111.57	111.57	111.25	110.75	109.75	0.00	0.32	0.82	1.82
	81.17	81.17	80.85	80.35	79.35	0.00	0.32	0.82	1.82
4	101.31	101.31	100.99	99.99	98.99	0.00	0.32	1.32	2.32
	142.72	142.72	142.40	141.40	140.40	0.00	0.32	1.32	2.32
	56.59	56.59	56.27	55.27	54.27	0.00	0.32	1.32	2.32
	59.32	59.32	59.00	58.00	57.00	0.00	0.32	1.32	2.32
	82.11	82.11	81.79	80.79	79.79	0.00	0.32	1.32	2.32

5	35.54	35.22	34.90	33.90	32.90	0.32	0.64	1.64	2.64
	58.75	58.43	58.11	57.11	56.11	0.32	0.64	1.64	2.64
	37.00	36.68	36.36	35.36	34.36	0.32	0.64	1.64	2.64
	47.55	47.23	46.91	45.91	44.91	0.32	0.64	1.64	2.64
	29.92	29.60	29.28	28.28	27.28	0.32	0.64	1.64	2.64
6	71.55	71.23	70.91	69.91	69.41	0.32	0.64	1.64	2.14
	81.78	81.46	81.14	80.14	79.64	0.32	0.64	1.64	2.14
	81.46	81.14	80.82	79.82	79.32	0.32	0.64	1.64	2.14
	130.92	130.60	130.28	129.28	128.78	0.32	0.64	1.64	2.14
	25.53	25.21	24.89	23.89	23.39	0.32	0.64	1.64	2.14

The elevation of each soil layer listed in the table is the bottom elevation of each layer; the depth of each layer is the depth from the ground surface to the bottom of the corresponding layer.

Table 5.4 Eight cases with different horizontal pseudo-acceleration coefficients applied in the calculation

Case	**Horizontal pseudo-acceleration coefficient, k_{eq}**	**Remark**
1	0	without seismic loading
2	0.1	Seed (1979)
3	0.15	great earthquake, Corps of Engineers (1982)
4	0.2	Seed (1979)
5	0.238	1/3 of PHGA, Marcuson and Franklin (1983)
6	0.358	1/2 of PHGA, Marcuson and Franklin (1983); Hynes-Griffin and Franklin (1984)
7	0.477	2/3 of PHGA
8	0.5	catastrophic earthquakes, Terzaghi (1950)

5.3 Results and discussion

In general, the predicted areas with F_S less than 1.0 are considered as unstable and the predicted areas with F_S more than 1.0 are regarded as stable area. In order to evaluate the performance of the calculation results, a more detailed classification of slope stability and instability was introduced (Table 5.5). In this work, eight cases Areas with F_S less than 0.75 and between 0.75 and 1.0 indicate the very unstable and unstable areas. In this work, the calculation of case 1 without seismic loading was conducted to simulate the state before the Iburi earthquake occurrence. Case 2 to case 8 with the increasing horizontal seismic coefficients were conducted to check the performance of the calculated results. By validating using the coseismic landslide inventory, a proper horizontal seismic coefficient range suitable for slope stability assessment can be obtained.

Table 5.5 Classifications of slope stability and instability based on Ray and De Smedt (2009) and Teixeira et al. (2015)

Stability classification	**Factor of safety**	**Slope stability class**
1	Fs≤0.75	very unstable
2	0.75<Fs≤1	unstable
3	1<Fs≤1.25	quasi stable
4	1.25<Fs≤1.5	stable
5	Fs>1.5	very stable

The factor-of-safety map calculated by Scoops3D is grid-based, thus, GIS can be applied to validate the calculation result. Figure 5.10 shows the factor-of-safety maps calculated with different horizontal pseudo-acceleration coefficients. In case 1, the factor-of-safety map indicates that the whole study area is in stable state without seismic loading and only very limited areas, i.e., the Tomisato sliding area and the eastern boundary of the study area, have high possibility for slope failure (Fig. 5.10a). Case 2 to case 8 illustrate that slope instability increases with the increase of horizontal pseudo-acceleration coefficients. A horizontal pseudo-acceleration coefficient of 0.5 (case 8) will result in that more than half of the whole study area is in unstable state. In order to quantitively evaluate to calculation results, landslide points distributed in each stability classes were extracted and areas of slope stability classes were calculated for eight cases. Figure 5.11 displays the cumulative landslide point percentage of the slope stability classes. For case 1, no landslide is predicted in the very unstable class and 99.8% of the coseismic landslides are distribute in the stable classes (quasi stable, stable and very stable). This is in well accordance with the real case. With the horizontal pseudo-acceleration coefficients of between 0.1 and 0.238 (case 2 to case 5), 6.1% to 22.2% of the Iburi landslides are spread in the unstable classes (very unstable and unstable), which is far from the satisfactory results. The cumulative landslide point percentage of unstable classes is 53.5% with the horizontal pseudo-acceleration coefficient of 0.358 (1/2 of PHGA) and the corresponding cumulative class area percentage is 31.5% with same seismic coefficient. In case 7 and 8, the calculation results seem to be perfect as 75.7% and 80.6% of the triggered landslides are located in the unstable classes. However, the cumulative percentage of the unstable classes in case 7 and case 8 are as high 49.1% and 53.4%. Thus, the seismic coefficients applied in case 7 and case 8 (especially in case 8) may result in overestimation of the slope instability.

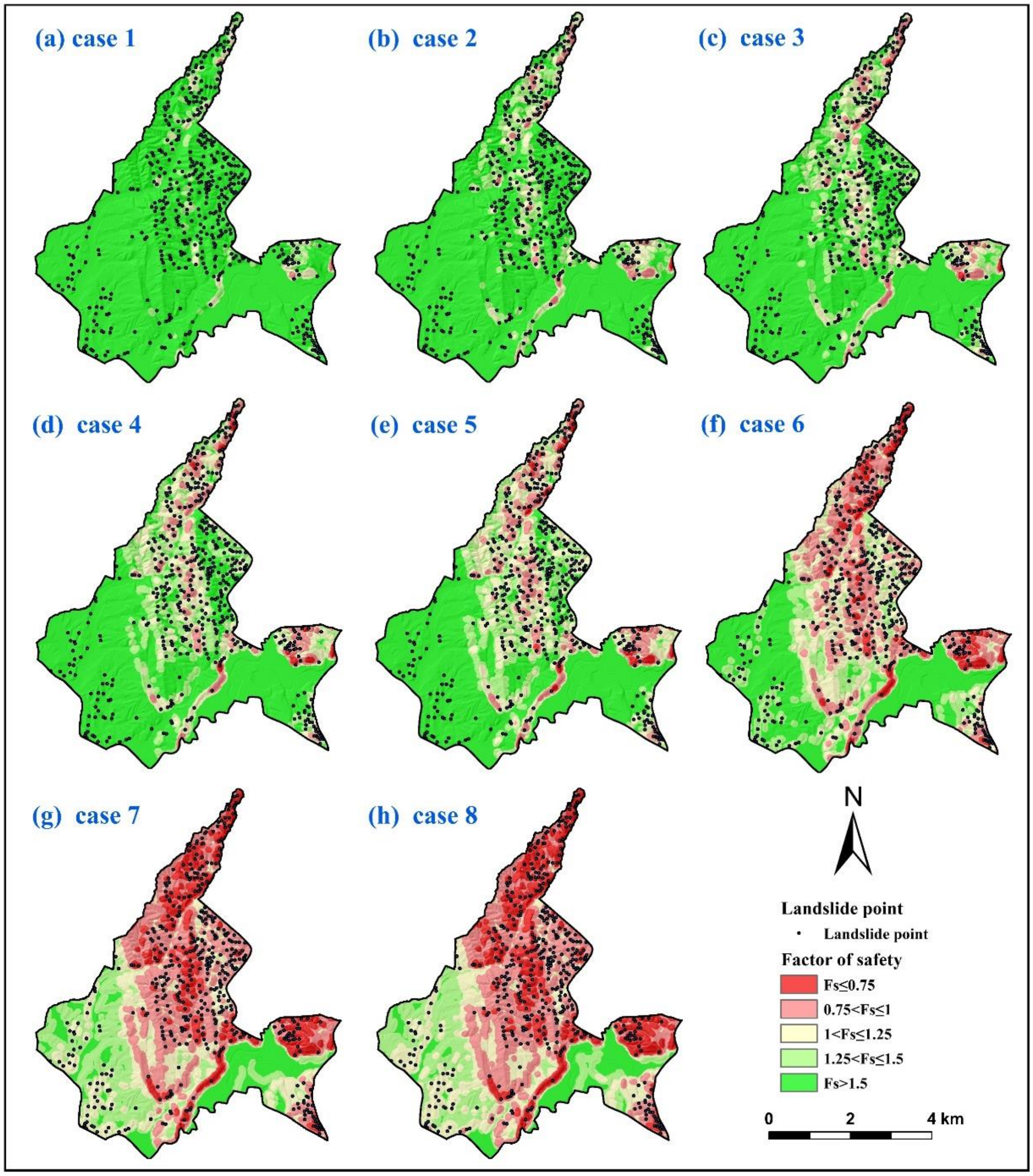

Fig. 5.10 Factor-of-safety maps calculated with different horizontal pseudo-acceleration coefficients

The sizes of Iburi landslides in the study area range from 77 m^2 to 115,214 m^2, therefore the landslide area should be also considered in the validation of the calculated results. Besides, the aforementioned validation method can not include the false predicted area, i.e., the predicted unstable area in the area where no slope failure occurs during the Iburi earthquake. In view of this, the example contingency table for a two-class problem, also termed as an error matrix (Stehman 1997) or a confusion matrix, were utilized to validate the calculation results. Even though the factor-of-safety map calculated by Scoops3D is for the whole potential sliding area, each grid cell of factor-of-safety map has a unique value representing the factor of safety and all grid cells can be determined as one of the four elements (true positive, false negative, false positive or true negative) in Figure 5.12. The grid cell computed to be unstable is counted as true positive if it falls in real landsliding area and it is counted as false positive if it falls outside real landsliding area; correspondingly, the grid cell calculated as stable is counted as a true negative if it is located outside the triggered landslides and it is counted as a false negative if it is located within the triggered landslides (Godt et al. 2008).

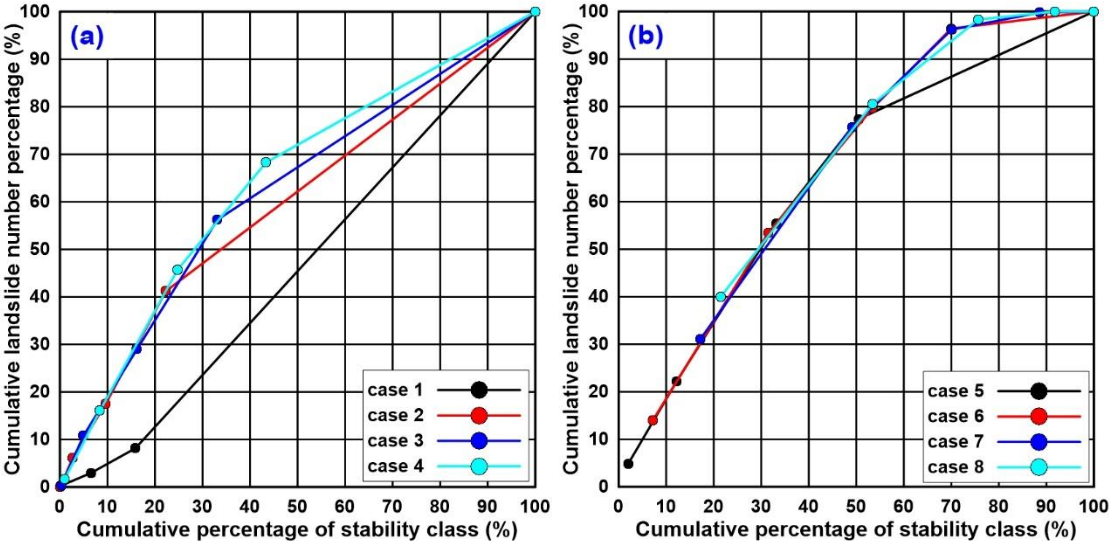

Fig. 5.11 Cumulative landslide percentages of five stability classes for eight cases

The example contingency table of eight cases in this work is listed in Table 5.6, and the values in the column TP, FN, TN, P, N and P+N are the grid cell counts of corresponding cases. Similar with Figure 5.10a, the TPR for case 1 without seismic loading is as low as 0.002, which means very few landslides are correctly predicted. The TPRs of cases 2 to 8 increase from 0.07 to 0.87 as the seismic coefficients increase from 0.1 to 0.5, but the FPRs also increase from 0.02 to 0.49. The high FPR of case 8 indicates almost half of the area without landslide occurrence during the Iburi earthquake was predicted as unstable area. In general, a perfect result should meet the requirements of maximum TPR and minimum FPR when the TPR/FPR is more than 1 (Fawcett 2006). However, in most models a higher TPR is accompanied by a higher FPR. The perfect predicted results should incorporate high veracity and acceptable error rate. The TPR of case 6 is approximately same to the predicted results using Scoops3D in loess area, while the FPR is much lower than that predicted in loess area ((Xin et al. 2018)). The horizontal seismic coefficient of between 1/2 PHGA to 2/3 PHGA seems to be effective to obtain good results in pyroclastic fall deposits under seismic loading.

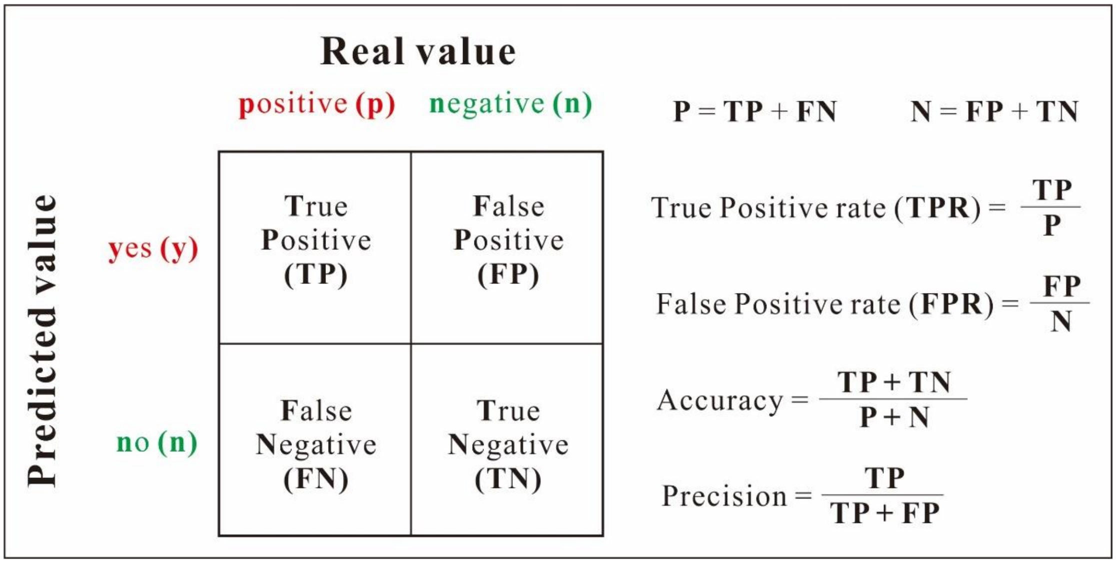

Fig. 5.12 Schematic diagram of the confusion matrix (modified from Fawcett (2006))

The occurrence of coseismic landslides in area with relatively low slope angle is one of the typical characteristics during the Iburi earthquake and the existence of (act) faults also play an important role in the occurrence of the Iburi landslides. More than 50 landslides are distributed in the flat west part of the study area and these landslides are not well predicted even with a horizontal seismic coefficient of 0.5. The occurrence of these landslides in flat topography decreases the predicted accuracy. Even so, a horizontal seismic coefficient between 1/2 PHGA to 2/3 PHGA can correctly predict 53.5% to 75.7% of the landslide points, and correctly predict 63.5% to 82.7% of the total landsliding area (represented by the TPR).

Table 5.6 Calculation results of eight cases with or without seismic loading

Case	**TP**	**FN**	**FP**	**TN**	**P**	**N**	**P+N**	**TPR**	**FPR**	**Accuracy**	**Precision**	**TPR/FPR**
1	7,900	3,187,025	65,900	24,448,075	3,194,925	24,513,975	27,708,900	0.0025	0.0027	0.88	0.11	0.92
2	232,200	2,962,725	510,325	24,003,650	3,194,925	24,513,975	27,708,900	0.07	0.02	0.87	0.31	3.49
3	403,975	2,790,950	964,325	23,549,650	3,194,925	24,513,975	27,708,900	0.13	0.04	0.86	0.30	3.21
4	695,300	2,499,625	1,635,675	22,878,300	3,194,925	24,513,975	27,708,900	0.22	0.07	0.85	0.30	3.26
5	964,125	2,230,800	2,412,175	22,101,800	3,194,925	24,513,975	27,708,900	0.30	0.10	0.83	0.29	3.07
6	2,029,700	1,165,225	6,699,625	17,814,350	3,194,925	24,513,975	27,708,900	0.64	0.27	0.72	0.23	2.32
7	2,643,400	551,525	10,950,050	13,563,925	3,194,925	24,513,975	27,708,900	0.83	0.45	0.58	0.19	1.85
8	2,768,200	426,725	12,038,300	12,475,675	3,194,925	24,513,975	27,708,900	0.87	0.49	0.55	0.19	1.76

CHAPTER 6

CONCLUSIONS

The Iburi earthquake sequence triggered 5,625 landslides in an elliptic area covering approximately 1,557 km^2. Most of the coseismic landslides are coherent shallow debris slides and disrupted mobilization of valley fill occurred in pyroclastic fall deposits originating from the eruption of the Tarumae Volcano. Only one deep-seated landslide (also the largest landslide) occurred in the Neogene sedimentary rocks was determined. The majority of landslides are characterized as being of small to medium size with an area between 1,000 m^2 and 10,000 m^2, in area with a base of Neogene sedimentary rocks (N2sn and N3sn). Controlled by seismic factors, 89.6% of the coseismic landslides are distributed in classes with seismic intensity between 7.0 and 8.0 and 86.2% are concentrated in an area with PGA of 0.4 g to 0.7 g. In addition, the precipitation that occurred in August also aggravated the occurrence of landslide during the intense earthquake. Several impressive characteristics of the coseismic landslides were obtained in the Iburi earthquake:

1. Sliding zone liquefaction of the Ta-d pumice layers is a distinguishing feature observed in the Iburi landslides. The crushed and liquified pumice layers resulted in the high mobility and long run-out distance of the coseismic landslides.

2. Their extremely high concentration: 3,638 landsides (64.7%) are concentrated in an ellipse occupying about 173 km^2 and corresponding to 21.0 per km^2. This phenomenon is uncommon in comparison to previously studied events.

3. An approximately orthogonal spatial distribution and preferred slip orientation: The NNW/SSE extending distribution and southerly (S, SW, and SE) preferred inclination of the total affected area demonstrate the influence and impact of regional tectonics on the spatial distribution and slip orientation of landslides.

4. The frequent occurrence and high concentration of landslides occurring in hilly terrain: 4,357 landslides occurred at elevations between 100 m and 250 m, corresponding to the LC of 7.1 per km^2, and the LC of 4,829 coseismic landslides with mean slope angle between 15° and 35° is 8.4 per km^2.

5. Coseismic landslide occurrence in old landslide area: 109 coseismic landslides occupying 2.6% of the coseismic landslides area occurred in the old landslide area, which may be attributed to the extraordinary characteristics of stratified and cyclothemic pyroclastic fall deposits around the study area.

In this work, GIS was applied to process the input the ground surface and soil layers as well as the output factor-of-safety maps, and Scoops3D was employed to conduct the three-dimensional seismic slope stability calculation. The soil structure of the study area was constructed based on the isopachs of the pyroclastic fall deposits and the groundwater configuration was assumed as a piezometric surface located at the bottom of the Ta-d layer. Regional slope stability assessment of eight cases with different horizontal pseudo-acceleration coefficients were conducted to simulate the states with or without a seismic loading. 345 coseimic landslides in the study occurred during the Iburi earthquake were utilized to validate the accuracy of the calculated results.

The calculated result without seismic loading in case 1 shows high consistency with the real case and more than 99.8% of the study area is in stable state. The horizontal seismic coefficients of 0.1 to 0.238 applied in the slope stability computation result in 6.1% to 22.2% of total landslide number and the corresponding TPR and FPR range from 0.07 to 0.3 and 0.02 to 0.1. Obviously, these calculation results are far from satisfactory. The predicted result with a seismic coefficient of 0.5 manifests 80.6% of the triggered landslides with landslide area percentage of 86.6% are correctly predicted. But this predicted result overestimate the unstable area as the FPR value of this case is as high as 0.49. Based on the modelled results of case 6 and case 7, a horizontal pseudo-acceleration coefficient between 0.358 (1/2 of PHGA) and 0.477 (2/3 of PHGA) may be suitable for slope stability evaluation since 53.5% to 75.7% of the total landslide (landslide point) can be predicted and 63.5% to 82.7% of the total sliding area can be modelled. The computed result a horizontal pseudo-acceleration coefficient between 1/2 and 2/3 of PHGA is satisfactory, especially in hilly regions. Besides, the factor-of-safety map in Figures 10f and 10g indicate that two most destructive landslides, i.e., the Tomisato landslide and the Yoshinoya landslide are correctly predicted.

REFERENCES

Arita K, Ikawa T, Ito T, Yamamoto A, Saito M, Nishida Y, Satoh H, Kimura G, Watanabe T, Ikawa T, Kuroda T (1998) Crustal structure and tectonics of the Hidaka Collision Zone, Hokkaido (Japan), revealed by vibroseis seismic reflection and gravity surveys. Tectonophysics 290(3-4):197-210

Baum RL, Savage WZ, Godt JW (2002) TRIGRS-A Fortran program for transient rainfall infiltration and grid-based regional slope-stability analysis. U.S. Geological Survey Open-File Report 02-0424

Brien DL, Reid ME (2007) Modeling 3-D slope stability of coastal bluffs using 3-D ground-water flow, southwestern Seattle, Washington. U.S. Geological Survey Scientific Investigations Report 2007–5092

Cabinet office (2018) About damage situation on the 2018 Hokkaido Eastern Iburi Earthquake, 29 October 2018, 17:30

Cavoundis S (1987) On the ratio of factors of safety in slope stability analyses. Geotechnique 37(2): 207-210

Chigira M, Yagi H (2006) Geological and geomorphological characteristics of landslides triggered by the 2004 Mid Niigata prefecture earthquake in Japan. Engineering Geology 82(4):202-221

Collins BD, Jibson RW (2015) Assessment of existing and potential landslide hazards resulting from the April 25, 2015 Gorkha, Nepal earthquake sequence. U.S. Geological Survey Open File Report 2015–1142, Reston, VA

Collins BD, Kayen R, Tanaka Y (2012) Spatial distribution of landslides triggered from the 2007 Niigata Chuetsu–Oki Japan Earthquake. Engineering geology 127:14-26

Corps of Engineers (1982) Slope Stability Manual EM-1110-2-1902. Washington, D. C.: Department of the Army, Office of the Chief of Engineers

Dai F, Xu C, Yao X, Xu L, Tu X, Gong Q (2011) Spatial distribution of landslides triggered by the 2008 Ms 8.0 Wenchuan earthquake, China. Journal of Asian Earth Sciences 40(4):883-895

Del Soldato M, Solari L, Poggi F, Raspini F, Tomás R, Fanti R, Casagli N (2019) Landslide-Induced Damage Probability Estimation Coupling InSAR and Field Survey Data by Fragility Curves. Remote Sensing 11(12):1486

Duncan JM (1996) State of the art: limit equilibrium and finite-element analysis of slopes. Journal of Geotechnical engineering 122(7):577-596

Fawcett T (2006) An introduction to ROC analysis. Pattern recognition letters 27(8):861-874

Fukuoka H, Sassa K, Scarascia-Mugnozza G (1997) Distribution of landslides triggered by the 1995 Hyogo-ken Nanbu earthquake and long runout mechanism of the Takarazuka Golf Course landslide. Journal of Physics of the Earth 45(2):83-90

Furukawa R, Nakagawa M (2010) G geological map of Tarumae volcano. Geological Survey of Japan, AIST

Gnyawali KR, Maka S, Adhikari BR, Chamlagain D, Duwal S, Dhungana AR (2016) Spatial implications of earthquake induced landslides triggered by the April 25 Gorkha earthquake Mw 7.8: preliminary analysis and findings. International conference on earthquake engineering and post disaster reconstruction planning 24–26 April, 2016, Bhaktapur, Nepal:50-58

Godt JW, Baum RL, Savage WZ, Salciarini D, Schulz WH, Harp EL (2008) Transient deterministic shallow landslide modeling: requirements for susceptibility and hazard assessments in a GIS framework. Engineering Geology 102(3-4):214-226.

Gorum T, Fan X, van Westen CJ, Huang RQ, Xu Q, Tang C, Wang G (2011) Distribution pattern of earthquake-induced landslides triggered by the 12 May 2008 Wenchuan earthquake. Geomorphology 133(3-4):152-167

Gratchev IB, Towhata I (2011) Analysis of the mechanisms of slope failures triggered by the 2007 Chuetsu Oki earthquake. Geotechnical and Geological Engineering 29(5):695-708

Guo C, Montgomery DR, Zhang Y, Wang K, Yang Z (2015) Quantitative assessment of landslide susceptibility along the Xianshuihe fault zone, Tibetan Plateau, China. Geomorphology 248:93-110

Guzzetti F, Malamud BD, Turcotte DL, Reichenbach P (2002) Power-law correlations of landslide areas in central Italy. Earth and Planetary Science Letters 195(3-4):169-183

Harp EL, Jibson RW (1996) Landslides triggered by the 1994 Northridge, California, earthquake. Bulletin of the Seismological Society of America 86(1B):S319-332

Hays J (2010) Facts and details. Earthquakes and Japan

Hirose W, Kawakami G, Kase Y, Ishimaru S, Koshimizu K, Koyasu H, Takahashi R (2018) Preliminary report of slope movements at Atsuma Town and its surrounding areas caused by the 2018 Hokkaido Eastern Iburi Earthquake. Report of the Geological Survey of Hokkaido 90: 33-44

Hokkaido Prefectural Government (2018) Disaster Verification Committee for the 2018 Hokkaido Eastern Iburi Earthquake, Reference 3, Summary of damage

Hovius N, Stark CP, Allen PA (1997) Sediment flux from a mountain belt derived by landslide mapping. Geology 25(3):231-234

Hungr O (1987) An extension of Bishop’s simplified method of slope stability analysis to three dimensions. Geotechnique 37(1):113–117

Hynes-Griffin ME, Franklin AG (1984) Rationalizing the seismic coefficient method. U.S. Army Corps of Engineers Waterways Experiment Station, Vicksburg, Mississippi, Miscellaneous Paper GL-84-13 21 pp

Japan Meteorological Agency (2018) On the operation status of observation instruments in Hokkaido

Keefer DK (1998) The Loma Prieta, California, Earthquake of October 17, 1989: Landslides. U.S. Geological Survey Professional Paper 1551-C 185 pp

Keefer DK (2000) Statistical analysis of an earthquake-induced landslide distribution—the 1989 Loma Prieta, California event. Engineering geology 58(3-4):231-249

Keefer DK (2002) Investigating landslides caused by earthquakes–a historical review. Surveys in geophysics 23(6):473-510

Khazai B, Sitar N (2003) Evaluation of factors controlling earthquake-induced landslides caused by Chi-Chi earthquake and comparison with the Northridge and Loma Prieta events. Engineering geology 71(1-2):79-95

Kimura G (1983) Collision tectonics in Hokkaido and Sakhalin. Accretion tectonics in the Circum-Pacific regions:123-134

Kimura G (1994) The latest Cretaceous-early Paleogene rapid growth of accretionary complex and exhumation of high pressure series metamorphic rocks in northwestern Pacific margin. Journal of Geophysical Research: Solid Earth 99 (B11):22147-22164

Kinoshita S (1998) Kyoshin net (K-net). Seismological Research Letters 69(4):309-32

Lam L, Fredlund DG (1993) A general limit-equilibrium model for three-dimensional slope stability analysis. Can Geotech J 30:905–919

Liu L, Yin K, Xu Y, Lian Z, Wang N (2018) Evaluation of regional landslide stability considering rainfall and variation of water level of reservoir. Chinese Journal of Rock Mechanics and Engineering 37(2):403-414

Machida H, Arai F (2003) Atlas of Tephra in and around Japan (revised edition). University of Tokyo Press, Tokyo 336 pp

Malamud BD, Turcotte DL, Guzzetti F, Reichenbach P (2004) Landslides, earthquakes, and erosion. Earth and Planetary Science Letters 229(1-2):45-59

Marcuson WF, Franklin AG (1983) Seismic design, analysis, and remedial measures to improve stability of existing earth dams-Corps of Engineers Approach. In Seismic Design of Embankments and Caverns, T.R. Howard, Ed., New York, ASCE 65-78 pp

Meunier P, Hovius N, Haines JA (2008) Topographic site effects and the location of earthquake induced landslides. Earth and Planetary Science Letters 275(3-4):221-232

Miura S, Yagi K (2005) Geotechnical properties of volcanic ash soils in Hokkaido. Soil mechanics and foundation engineering 53(5):5-7

Miura S, Yagi K, Asonuma T (2003) Deformation-strength evaluation of crushable volcanic soils by laboratory and in-situ testing. Soils and Foundations 43(4):47-57

Montgomery DR, Dietrich WE (1994) A physically based model for the topographic control on shallow landsliding. Water resources research 30(4):1153-1171

Nakagawa M, Amma-Miyasaka M, Miura D, Usewa S (2018) Tephrostatigraphy in Ishikari Lowland, Southwestern Hokkaido: Eruption history of the Shikotsu-Toya volcanic field. The Journal of the Geological Society of Japan 124(7):473-489

Normile D (2018) Slippery volcanic soils blamed for deadly landslides during Hokkaido earthquake. (https://www.sciencemag.org/news/2018/09/slippery-volcanic-soils-blamed-deadly-landslides-during-hokkaido-earthquake)

Okamura Y, Tsujino T, Arai K, Sasaki T, Satake K, Joshima M (2008) Fore arc structure and plate boundary earthquake sources along the southwestern Kuril subduction zone. Journal of Geophysical Research: Solid Earth 113(B6)

Organization for Cross-regional Coordination of Transmission Operation, Japan (2018) The 1st Evaluation Committee on large scale blackout associated with the 2018 Hokkaido Eastern Iburi Earthquake, reference 4-1, About events from earthquake occurrence to blackout,"

Ozaki M, Taku K (2014) 1:200,000 Land geological map in the Ishikari Depression and its surrounding area with explanatory note. Seamless Geoinformation of Coastal Zone "Southern Coastal Zone of the Ishikari Depression", Seamless Geological Map of Costal Zone S-4, Geological Survey of Japan ALST

Pack RT, Tarboton DG, Goodwin CN (1998) The SINMAP approach to terrain stability mapping. Proceedings of 8th Congress of the International Association of Engineering Geology, Vancouver, British Columbia, Canada 1157-1165 pp

Papathanassiou G, Valkaniotis S, Ganas A, Pavlides S (2013) GIS-based statistical analysis of the spatial distribution of earthquake-induced landslides in the island of Lefkada, Ionian Islands, Greece. Landslides 10(6):771–783

Petley D (2018) Landslides triggered by the 6th September 2018 Hokkaido earthquake (https://blogs.agu.org/landslideblog/2018/09/06/landslides-6th-september-2018-hokkaido-earthquake/)

Qi S, Xu Q, Lan H, Zhang B, Liu J (2010) Spatial distribution analysis of landslides triggered by 2008.5.12 Wenchuan Earthquake, China. Engineering geology 116(1-2):95-108

Ray RL, De Smedt F (2009) Slope stability analysis on a regional scale using GIS: a case study from Dhading, Nepal. Environmental geology 57(7):1603-1611

Reid ME, Christian SB, Brien DL, Henderson ST (2015) Scoops3D-software to analyze three-dimensional slope stability throughout a digital landscape. U.S. Geological Survey; Volcano Science Center: Menlo Park, CA, USA

Reid ME, Keith TE, Kayen RE, Iverson NR, Iverson RM, Brien DL (2010) Volcano collapse promoted by progressive strength reduction: new data from Mount St. Helens. Bulletin of volcanology 72(6):761-766

Reid ME, Sisson TW, Brien DL (2001) Volcano collapse promoted by hydrothermal alteration and edifice shape, Mount Rainier, Washington. Geology 29(9):779-782

Sassa K, Fukuoka H, SCARASCIA-MUGNOZZA GA (1996) Earthquake-induced-landslides: distribution, motion and mechanisms. Soils and Foundations 36 (Special):53-64

Sassa K, Fukuoka H, Wang F, Wang G (2005) Dynamic properties of earthquake-induced large-scale rapid landslides within past landslide masses. Landslide 2(2):125-134

Sato HP, Sekiguchi T, Kojiroi R, Suzuki Y, Iida M (2005) Overlaying landslides distribution on the earthquake source, geological and topographical data: the Mid Niigata prefecture earthquake in 2004, Japan. Landslides 2(2):143-152

Schuster RL (1996) Landslides: investigation and mitigation. chapter 2-socioeconomic significance of landslides. Transportation research board special report 247

Seed HB (1979) Considerations in the earthquake-resistant design of earth and rockfill dams. Geotechnique 29(3):215-263

Spencer E (1967) A method of analysis the stability of embankments assuming parallel inter-slice forces. Geotechnique 17(1):11–26

Stark CP, Hovius N (2001) The characterization of landslide size distributions. Geophysical Research Letters 28(6):1091-1094

Stehman SV (1997) Selecting and interpreting measures of thematic classification accuracy. Remote sensing of Environment 62(1):77-89

Tajika J, Ohtsu S, Inui T (2016) Interior structure and sliding process of landslide body composed of stratified pyroclastic fall deposits at the Apporo 1 archaeological site, southeastern margin of the Ishikari Lowland, Hokkaido, North Japan. The Journal of the Geological Society of Japan 122(1):23-35

Takahashi H, Kimura R (2019) The 2018 Hokkaido Eastern Iburi Earthquake and its Aftermath. Journal of Disaster Research 14:1-3

Takashima R, Nishi H, Yoshida T (2002) Geology, petrology and tectonic setting of the Late Jurassic ophiolite in Hokkaido, Japan. Journal of Asian Earth Sciences 21(2):197-215

Tamaki M, Kusumoto S, Itoh Y (2010) Formation and deformation processes of late Paleogene sedimentary basins in southern central Hokkaido, Japan: paleomagnetic and numerical modeling approach. Island Arc. 19(2):243-258

Teixeira M, Bateira C, Marques F, Vieira B (2015) Physically based shallow translational landslide susceptibility analysis in Tibo catchment, NW of Portugal. Landslides 12(3):455-468

Terzaghi K (1950) Mechanisms of Landslides. Engineering Geology (Berkeley) Volume, Geological Society of America

Tran TT, Alvioli M, Lee G, An HU (2018) Three-dimensional, time-dependent modeling of rainfall-induced landslides over a digital landscape: a case study. Landslides15:1071-1084

Vallance JW, Schilling SP, Devoli G, Reid ME, Howell MM, Brien DL (1998) Lahar Hazards at Casita and San Cristóbal Volcanoes, Nicaragua. Retrieved from Vancouver, Washington U.S.A. U.S. Geological Survey 1-24 pp

Vallance JW, Schilling SP, Devoli G, Reid ME, Howell MM, Brien DL (2004) Lahar hazards at casita and San Cristóbal volcanoes, Nicaragua. U.S. Geological Survey Open-File Report 2001–468

Wang F, Fan X, Yunus AP, Subramanian SS, Alonso-Rodriguez A, Dai L, Xu Q, Huang R (2019) Coseismic landslides triggered by the 2018 Hokkaido, Japan (Mw 6.6), earthquake: spatial distribution, controlling factors, and possible failure mechanism. Landslides:1-16

Wang FW (1999) An experimental study on grain crushing and excess pore pressure generation during shearing of sandy soils: A key factor for rapid landslide motion. PhD thesis of Kyoto University. Kyoto University Research Information Repository

Wang H, Sassa K, Xu W (2007) Analysis of a spatial distribution of landslides triggered by the 2004 Chuetsu earthquakes of Niigata Prefecture, Japan. Natural Hazards 41(1):43

Wang WN, Nakamura H, Tsuchiya S, CHEN CC (2002) Distributions of landslides triggered by the Chi-chi Earthquake in Central Taiwan on September 21, 1999. Landslides 38(4):318-326

Wartman J, Dunham L, Tiwari B, Pradel D (2013) Landslides in Eastern Honshu Induced by the 2011 Tohoku Earthquake. Bulletin of the Seismological Society of America 103(2B):1503-1521

Whitehouse IE, Griffiths GA (1983) Frequency and hazard of large rock avalanches in the central Southern Alps, New Zealand. Geology 11(6):331-334

Wu W, Sidle RC (1995) A distributed slope stability model for steep forested basins. Water resources research 31(8):2097-2110

Xin X, Zhang F (2018) Application of a 3D deterministic model for predicting shallow loess landslide stability. Chinese Journal of Engineering 40(4):397-406

Xu C, Ma S, Tan Z (2018) Landslides triggered by the 2016 Mj 7.3 Kumamoto, Japan, earthquake. Landslides 15(3):551-564

Xu C, Xu X, Yao X, Dai F (2014) Three (nearly) complete inventories of landslides triggered by the May 12, 2008 Wenchuan Mw 7.9 earthquake of China and their spatial distribution statistical analysis. Landslides 11(3):441-461

Xu Q, Zhang S, Li W (2011) Spatial distribution of large-scale landslides induced by the 5.12 Wenchuan earthquake. J Mt Sci 8(2):246–260

Yagi H, Sato G, Higaki D, Yamamoto M, Yamasaki T (2009) Distribution and characteristics of landslides induced by the Iwate–Miyagi Nairiku Earthquake in 2008 in Tohoku District, Northeast Japan. Landslides 6(4):335-344

Yamagishi H, Yamazaki F (2018) Landslides by the 2018 Hokkaido Iburi-Tobu Earthquake on September 6. Landslides 15(12):2521-2524

Yin Y, Wang FW, Sun P (2009) Landslide hazards triggered by the 2008 Wenchuan earthquake, Sichuan, China. Landslides 6(2):139-152

Zhang Y, Dong S, Hou C, Guo C, Yao X, Li B, Du J, Zhang J (2013) Geohazards induced by the Lushan Ms7. 0 earthquake in Sichuan Province, Southwest China: typical examples, types and distributional characteristics. Acta Geologica Sinica-English Edition 87(3):646-657

Zhang Y, Yao X, Xiong T, Ma Y, Hu D, Yang N, Guo C (2010) Rapid identification and emergency investigation of surface ruptures and geohazards induced by the Ms 7.1 Yushu Earthquake. Acta Geologica Sinica-English Edition 84(6):1315-1327